

A submillimetre survey of the star-formation history of radio galaxies

E. N. Archibald^{1,2}*, J. S. Dunlop², D. H. Hughes^{2,3}, S. Rawlings⁴, S. A. Eales⁵, and R. J. Ivison⁶

¹Joint Astronomy Centre, 660 N. A‘ohōkū Place, University Park, Hilo, Hawaii, 9620, USA

²Institute for Astronomy, University of Edinburgh, Blackford Hill, Edinburgh, EH9 3HJ, Scotland

³Instituto Nacional de Astrofísica, Óptica y Electrónica (INAOE), Apartado Postal 51 y 216, 72000 Puebla, Pue., Mexico

⁴Astrophysics, Department of Physics, Keble Road, Oxford, OX1 3RH, England

⁵Department of Physics and Astronomy, University of Wales Cardiff, P.O. Box 913, Cardiff, CF2 3YB, Wales

⁶Department of Physics & Astronomy, University College London, Gower Street, London, WC1E 6BT, England

arXiv:astro-ph/0002083v2 3 Nov 2000

Accepted ; Received ; in original form

ABSTRACT

We present the results of the first major systematic submillimetre survey of radio galaxies spanning the redshift range $1 < z < 5$. The primary aim of this work is to elucidate the star-formation history of this sub-class of elliptical galaxies by tracing the cosmological evolution of dust mass. Using SCUBA on the JCMT we have obtained 850- μ m photometry of 47 radio galaxies to a consistent rms depth of 1 mJy, and have detected dust emission in 14 cases. The radio galaxy targets have been selected from a series of low-frequency radio surveys of increasing depth (3CRR, 6CE, etc), in order to allow us to separate the effects of increasing redshift and increasing radio power on submillimetre luminosity. Although the dynamic range of our study is inevitably small, we find clear evidence that the typical submillimetre luminosity (and hence dust mass) of a powerful radio galaxy is a strongly increasing function of redshift; the detection rate rises from $\simeq 15$ per cent at $z < 2.5$ to $\gtrsim 75$ per cent at $z > 2.5$, and the average submillimetre luminosity rises at a rate $\propto (1+z)^3$ out to $z \simeq 4$. Moreover our extensive sample allows us to argue that this behaviour is not driven by underlying correlations with other radio galaxy properties such as radio power, radio spectral index, or radio source size/age. Although radio selection may introduce other more subtle biases, the redshift distribution of our detected objects is in fact consistent with the most recent estimates of the redshift distribution of comparably bright submillimetre sources discovered in blank field surveys. The evolution of submillimetre luminosity found here for radio galaxies may thus be representative of massive ellipticals in general.

Key words: galaxies: formation – galaxies: elliptical and lenticular, cD – dust, extinction – radio continuum: galaxies – galaxies: active – stars: formation

1 INTRODUCTION

Although large numbers of ‘normal’ galaxies have now been discovered out to $z \simeq 5$ (e.g. Steidel et al. 1999), radio galaxies continue to offer the best opportunity to study examples of *massive elliptical galaxies* (or the progenitors thereof) back to comparably early cosmic epochs. The reason for this is that a powerful radio source requires a massive black hole, and it is relatively certain that nowadays all such massive black holes reside in massive ellipticals (Magorrian et al.

1998; McLure et al. 1999). Thus radio selection offers a relatively efficient way of studying the properties of a sub-set of massive ellipticals as a function of cosmic epoch. Moreover this subset may well be representative of massive ellipticals in general, especially since it can be argued that a substantial fraction of all present-day ellipticals brighter than $2L^*$ must have been active at $z \simeq 2.5$ (Dunlop et al. 2000).

At low redshift, radio galaxies are dominated by well-evolved stellar populations (Nolan et al. 2000), have rather low dust/gas masses (Knapp & Patten 1991), and lie in the same region of the fundamental plane as normal inactive ellipticals (McLure et al. 1999; Dunlop et al. 2000). Moreover

* email: e.archibald@jach.hawaii.edu

current evidence suggests that they have evolved only passively since at least $z \simeq 1$ (Lilly & Longair 1984; McLure & Dunlop 2000). This, coupled with the relatively old ages derived for a few radio galaxies at $z \simeq 1.5$ (Dunlop 1999), points towards a high redshift of formation, $z > 3$, for the bulk of their stellar populations. This means that both the star-formation rate and gas mass in these galaxies should be a strongly increasing function of redshift as one approaches their primary formation epoch(s).

As has been argued by many authors, a massive starburst at high redshift is expected to produce rapid chemical enrichment and to be largely enshrouded in dust. Consequently, submillimetre luminosity should be a good indicator of the evolutionary state of an elliptical galaxy, being expected to peak roughly half-way through the production of a galaxy from primordial material (Eales & Edmunds 1996; Frayer & Brown 1997), or even earlier (i.e. as soon as the gas receives sufficient heating) given pre-existing enrichment (Hughes, Dunlop & Rawlings 1997). Indeed submillimetre luminosity, viewed as a tracer of gas mass, is arguably the best way to assess the evolutionary status of a massive galaxy. There are two reasons for this. Firstly, the sensitivity and bandwidth limitations of present-day instruments makes detecting molecular line emission from high-redshift objects extremely difficult. Secondly, in the case of radio galaxies, optical-UV measures may be confused by the direct or indirect effects of AGN activity.

The detectability of high-redshift radio galaxies at submillimetre wavelengths was first demonstrated by Dunlop et al. (1994), when they detected 4C41.17, at the time the most distant known galaxy at $z = 3.8$. However the observation, made with the single element bolometer detector UKT14 on the James Clerk Maxwell Telescope (JCMT), required 4 hours of integration in exceptional weather conditions. In fact, the sensitivity of UKT14 permitted only the most extreme objects to be detected at high redshift, and it was often a struggle to detect even those.

The advent of the Submillimetre Common-User Bolometer Array (SCUBA) on the JCMT offered the first real opportunity to rectify this situation. Although photometric observations do not fully exploit the multiplex advantage offered by an array camera, the individual bolometers in the SCUBA array offered almost an order of magnitude improvement in sensitivity over UKT14. This made it feasible to consider undertaking the first major submillimetre study of radio galaxies spanning a wide range of redshifts, and it is the results of the first major SCUBA survey of radio galaxies which we report here.

The layout of the paper is as follows: In Section 2 we give a more detailed overview of pre-existing submillimetre observations of radio galaxies, and explain the motivation for observing a sample of galaxies compiled from flux-limited radio surveys of increasing depth. The resulting sample is then described and summarized, before the results of our new submillimetre observations are presented in Section 3. Section 4 then gives details of the radio properties of each galaxy, and explains how the total and, where possible, core radio spectrum has been extrapolated to submillimetre wavelengths to estimate (or at least constrain) the potential level of non-thermal contamination at $850 \mu\text{m}$. The coverage of the radio-luminosity:redshift plane provided by our observed sample is presented in Section 5, and then in Section 6 we calculate the rest-frame $850\text{-}\mu\text{m}$ luminosities or upper limits for all the observed galaxies. In Section 7 we present a detailed statistical exploration of the evidence for genuine cosmological evolution of $L_{850\mu\text{m}}$ in our sample. Finally in Section 8 we conclude by considering our results in the context of the recently published blank-field submillimetre surveys.

We have deliberately confined this paper to a determination and discussion of the relative behaviour of submillimetre luminosity in our sample, and have postponed our analysis and interpretation of more model-dependent properties, such as inferred gas mass and galaxy age, to a subsequent paper.

1.1 Conventions

For clarity, we summarize here a number of conventions which have been adopted throughout this paper.

(i) For each galaxy in the sample, information has been collated from several references. Each reference has been given a code; for example, ER93 corresponds to Eales S.A., Rawlings S., 1993, *ApJ*, 411, 67. These codes are included in the bibliography.

(ii) Throughout the paper, upper limits are calculated using the following prescription: Consider an observation with signal S and standard error ε . If the signal is positive, the $n\text{-}\sigma$ upper limit is $S + (n \times \varepsilon)$. If the signal is negative, the $n\text{-}\sigma$ upper limit is $n \times \varepsilon$. It cannot be guaranteed that the upper limits taken from other papers were calculated in this manner.

(iii) For a power-law spectrum, the spectral index, α , is defined as $S_\nu \propto \nu^{-\alpha}$, where S_ν is the flux density at frequency ν . Thus, a radio synchrotron spectrum has a positive spectral index, and the Rayleigh-Jeans tail of a thermal spectrum has a negative spectral index.

(iv) The cosmological constant, Λ , is assumed to be zero throughout the paper.

2 PROJECT BACKGROUND AND SAMPLE SELECTION

2.1 Pre-existing millimetre/submillimetre detections of high-redshift radio galaxies

This work was carried out using SCUBA (Holland et al. 1999), the submillimetre bolometer array mounted on the JCMT. When the project was planned, SCUBA had not yet been commissioned, and only three high-redshift radio galaxies had been unambiguously detected at millimetre/submillimetre wavelengths: 6C0902+34 ($z=3.395$), 4C41.17 ($z=3.8$), and 8C1435+635 ($z=4.25$). While the millimetre observations of 6C0902+34 appeared to be dominated by non-thermal emission from the radio core (Downes et al. 1996), the observations of 4C41.17 and 8C1435+635 were striking in their similarity, with high emission levels attributed to the presence of large reservoirs of dust. The observed flux densities are detailed in Table 3.

4C14.17 and 8C1435+635 are both ultra-steep spectrum ($\alpha > 1.0$) radio galaxies, and both held the title, at

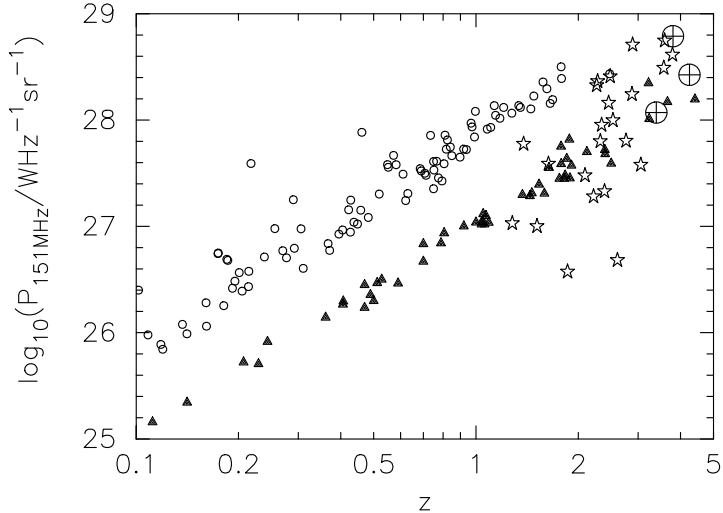


Figure 1. Radio luminosity-redshift plane as defined by radio surveys with successively deeper flux-density limits. Open circles denote galaxies from the 3C/3CRR survey and triangles denote galaxies from the 6CE survey. Stars indicate additional galaxies targeted as part of our SCUBA survey from the 4C*, 7CRS, 8C*, MIT-Green Bank MG*, and Texas TX* surveys. 4C41.17, 8C1435+635, and 6C0902+34 are each indicated by a large cross surrounded by a circle. As can be seen from this figure, they are some of the most distant, radio-luminous objects known. Note, 53W069 is too faint to appear on this version (and all subsequent versions) of the P-z plane. $H_0 = 50 \text{ km s}^{-1} \text{Mpc}^{-1}$, $\Omega_0 = 1.0$.

the time of their respective discovery, of being the most distant radio galaxy known. In addition, as can be seen in Figure 1, they are two of the most-luminous (at 151 MHz) radio sources known.

4C41.17 was detected at both 800 μm and 1300 μm (Dunlop et al. 1994; Chini & Krügel 1994), with the contribution from the non-thermal radio spectrum being less than a few percent at these wavelengths. Further support for a thermal emission mechanism came from the submillimetre spectral index: $\alpha_{1300}^{800} \sim -4$ (for self-absorbed synchrotron emission, $\alpha \geq -2.5$).

8C1435+635 was first detected at 1250 μm (Ivison 1995). As for 4C41.17, the contribution to the flux density from radio synchrotron emission is ~ 1 per cent. In addition, the flux density is roughly the same as that detected for 4C41.17 at 1300 μm .

Given its similarity to 4C41.17, and its tantalizing detection at 1250 μm , 8C1435+635 was a prime target for SCUBA. When this project was given its initial allocation of time, 8C1435+635 was the first object attempted, and we were able to study its submillimetre SED in unprecedented detail. Firm detections were made at 850 μm and 450 μm , confirming that the submillimetre spectrum rises well above the declining radio emission. Observations at 350 μm , 750 μm , and 175 μm resulted in upper limits to the continuum flux density; the last observation was made with the *Infrared Space Observatory* (ISO). In addition, a sensitive upper limit, $3\sigma < 5 \times 10^{10} \text{ K km s}^{-1} \text{pc}^2$ was obtained for the CO(4–3) line luminosity using the IRAM 30-m telescope. These data have been published in Ivison et al. (1998a); the observed flux densities (or limits) between $\lambda = 175\mu\text{m}$ and $\lambda = 1250\mu\text{m}$ are listed in Table 3.

Isothermal fits to the submillimetre spectrum suggest the majority of the emission comes from $2 \times 10^8 \text{ M}_\odot$ of dust with a temperature $40 \pm 5 \text{ K}$ and emissivity index $\beta = 2$ (as-

suming $H_0 = 50 \text{ km s}^{-1} \text{Mpc}$ and $\Omega_0 = 1$). However, higher temperatures, and correspondingly lower dust masses, are not ruled out by the data. The far-infrared luminosity implied by the preferred fit is $\text{LFIR} \sim 10^{13} \text{ L}_\odot$.

The amount of gas available for future star formation can be calculated from the dust mass if a gas-to-dust ratio is assumed. This assumption is notoriously uncertain; however, robust upper and lower limits on the amount of gas present can be calculated if the highest and lowest reasonable values for the ratio are considered. For 8C1435+635, such an analysis restricts the gas mass to $4 \times 10^{10} < M_{\text{gas}} < 1.2 \times 10^{12} \text{ M}_\odot$. In addition, if the dust is heated *solely* by star formation, the far-infrared luminosity indicates a star-formation rate of several thousand solar masses per year.

The dust masses responsible for the detections of 4C41.17 and 8C1435+635 are in excess of 10^8 M_\odot (Dunlop et al. 1994; Ivison 1995). This is at least an order of magnitude higher than what is observed for radio galaxies in the low-redshift Universe (Knapp & Patten 1991), indicating that, at $z = 4$, a significant amount of gas is yet to be converted into stars, suggesting that the host galaxies are not fully formed (Hughes et al. 1997).

2.2 Motivation for a complete sample of radio galaxies

The distant radio galaxies initially detected at submillimetre wavelengths are some of the most distant, radio-luminous objects known (Figure 1). On their own, they cannot be used to determine the evolutionary status of massive ellipticals at high redshift - their extreme submillimetre properties could be associated with either their redshift or the extreme nature of the radio source. There is a clear need for a proper

sample of radio galaxies spanning a range of radio luminosities and redshifts. If the radio luminosity-redshift plane (the P - z plane) is properly sampled, the effects of radio luminosity and cosmological evolution can be disentangled. The goal of this project was to study such a sample using SCUBA.

The galaxies were chosen based on their radio luminosity and their redshift. Before doing so, it was necessary to determine the frequency at which the radio luminosity should be calculated.

The radio luminosity of a classical double radio source is controlled by three key physical parameters: the bulk kinetic power in the jets, the age of the source (measured from the jet-triggering event) as it is observed on our light cone, and the environmental density (e.g. Blundell, Rawlings & Willott 1999). Provided the rest-frame frequency is high enough so that it exceeds the synchrotron self-absorption frequency, and low enough that the radiative timescale of electrons in the lobes is not so short that the lobes are completely extinguished, the selection effects inherent in any flux-limited sample lead to a reasonably close mapping between radio luminosity and jet power (e.g. Willott et al. 1999). These considerations render 151 MHz the rest-frame frequency of choice if one wishes to use radio luminosity to track the underlying jet power.

In any flux-density limited sample, there is a tight correlation between luminosity and redshift: for large distances, only the brightest objects will be observable - the faint objects will fall below the detection limit, and for small distances there are few bright sources in the small available cosmological volumes. Suppose galaxies were selected from a flux-limited radio survey and observed with SCUBA, with larger submillimetre flux densities measured for the high-redshift galaxies than for the low-redshift galaxies. It would be impossible to determine whether this was genuine cosmological evolution, or if the higher-redshift galaxies were brighter in the submillimetre because, for example, they are associated with objects with more powerful jets, perhaps because they are associated with more massive black holes and/or dark matter haloes. This problem can be overcome by using several radio surveys with different flux density limits to select our sample. The details of the redshift surveys of radio sources from which the sample was selected are described in Section 2.3. The region of the 151 MHz radio luminosity versus redshift plane covered by these surveys is shown in Figure 1.

2.3 The sample

Initially, a sample of radio galaxies was compiled from the 3C (Bennett 1962; Laing, Riley & Longair 1983 describe the doubly-revised version of the 3C sample, 3CRR) and 6CE (Eales 1985; Rawlings, Eales & Lacy 2000) radio surveys, for which complete redshift information exists. The galaxies were chosen to span a range of redshifts, $0.2 < z < 4.5$, but to lie in a narrow band of radio luminosity, $10^{27} \text{ W Hz}^{-1} \text{ sr}^{-1} < P_{151\text{MHz}} < 10^{29} \text{ W Hz}^{-1} \text{ sr}^{-1}$. This selection was made to minimise any radio luminosity bias and to determine if the submillimetre emission from radio galaxies truly evolves with redshift. Note that the top two decades in radio luminosity were chosen, allowing galaxies to be studied out to very high redshift. If there is a positive correlation between submillimetre emission and radio luminosity, per-

haps via galaxy mass, this choice should also maximise the chance of making detections.

In order to avoid strong radio synchrotron emission at submillimetre wavelengths, a further restriction was imposed on the selected sources: they were required to have steep radio spectra, with a spectral index $\alpha > 0.5$ for $\nu \sim 1 \text{ GHz}$. This selection criterion was aided by the fact that the radio galaxies were selected to be very luminous at 151 MHz - the most intrinsically luminous objects in low-frequency surveys tend to be steep-spectrum sources, whereas high-frequency surveys are biased towards flat-spectrum sources.

The 6CE galaxies have a declination limit $\delta < 40^\circ$. In order to minimise airmass, the criterion $\delta < 40^\circ$ was also imposed on the 3CRR catalogue sources.

As the project progressed, it became apparent that sources selected from the 3CRR and 6CE samples alone could not produce an even spread in radio luminosity within the chosen luminosity band. Additional sources, often with declinations $\delta > 40^\circ$, were added to the sample from:

(i) two flux-density limited radio surveys with complete, or near-complete, redshift information: the 7C Redshift Survey (7CRS) - Blundell et al. (2000); Willott et al. (2000); and the Leiden-Berkeley Deep Survey (LBDS) - Waddington et al. (2000) and references therein.

(ii) several 'filtered surveys' for which a filter, spectral index and/or angular size for example, has been applied to identify high redshift galaxies in a radio survey. The names and references for these filtered surveys are as follows: 4C* - Chambers et al. (1996); 6C* - Blundell et al. (1998); Jarvis et al. in preparation; 8C* - Lacy (1992); TX* (Texas) - van Ojik et al. (1996); and MG* (MIT-Green Bank) - Stern et al. (1999), Spinrad private communication.

Names, positions, and redshifts for the full sample observed with SCUBA are given in Table 1. In total, 47 radio galaxies were observed (27 from our original 3C/3CRR/6CE list). Note, for 3C356 two unresolved radio 'cores' have been detected within $5''$ of each other; they each have a galaxy at $z=1.079$ associated with them. It is not clear which galaxy is the host of the radio source; for further discussion of the merits of the two positions, refer to Best, Longair, & Röttgering (1997). SCUBA was pointed midway between the two identifications, and will have been offset $2''$ from the true position of the host galaxy; the flux lost should be negligible, < 5 per cent at $850 \mu\text{m}$.

3 SUBMILLIMETRE OBSERVATIONS

In this section, the results of all the submillimetre observations of the 47 galaxies in the sample are presented.

3.1 The SCUBA survey

SCUBA contains two bolometer arrays cooled to $\sim 75 \text{ mK}$ to achieve sky background-limited performance. Each array is arranged in a close-packed hexagon with a $2.3'$ instantaneous field of view. The diffraction-limited beamsizes delivered by the JCMT to SCUBA are $14.7''$ at $850 \mu\text{m}$ and $7.5''$ at $450 \mu\text{m}$; the bolometer feedhorns are sized for optimal coupling to the beams. Consequently, the long-wavelength (LW)

Table 1. Positions and redshifts of the radio galaxy sample observed with SCUBA. The parent samples, described in Section 2.3, are listed in Column 5. Column 6 (Pos. ID) indicates how the position was measured: ‘c’ - a radio core ID exists, ‘mc’ - a radio ID exists for a marginal radio core, ‘h’ - the radio ID is the mid-point of the hotspot peaks, ‘CSS’ - same as ‘h’ but for an extremely compact radio source, ‘O’ - an optical ID exists, ‘IR’ - an infrared ID exists, ‘HST’ - a Hubble Space Telescope ID exists. The position and redshift references are given in column 8, with references containing redshift information in bold. Notes: [§] 6C0930+38 is also referred to as 6C0929+38 in the literature. In the pre-release version of the 6C survey, astrometry indicated an RA of 09h 30m. However, in the final release of the survey, the position of the radio source appears as 09 29 59.7 +38 55 2. [#] The redshifts of 6C0919+38 and 6C1159+36 are not yet confirmed. For 6C0919+38, the estimate may not be too far off; for 6C1159+36, the redshift is based on a highly tentative Ly α emission line which is no longer considered secure (Rawlings et al. 2000). [†] For 3C356 the telescope was pointed at the midpoint of the two possible identifications (BLR97). [‡] The redshift of MG1744+18 is unpublished. A reference to a paper which quotes the unpublished value is included.

Common Name	IAU Name (B1950.0)	RA (B1950.0) (h m s)	Dec (B1950.0) (° ' '')	Parent Sample	Pos. ID	z	References.
6C0032+412	0032+412	00 32 10.73	+41 15 00.2	6C*	c	3.66	BRE98, Jprep
6C0140+326	0140+326	01 40 51.53	+32 38 45.8	6C*	h	4.41	BRE98, RLB96
4C60.07	0508+604	05 08 26.12	+60 27 17.0	4C*	mc, O	3.788	CMvB96, RvO97
4C41.17	0647+415	06 47 20.57	+41 34 03.9	4C*	c, O	3.792	COH94, RvO97
6C0820+36	0820+367	08 20 33.96	+36 42 28.9	6CE	c, IR	1.86	ERLG97, LLA95, REL00
5C7.269	0825+256	08 25 39.48	+25 38 26.5	7CRS	IR	2.218	ER96, W7CRS , BRR00
6C0901+35	0901+358	09 01 25.02	+35 51 01.8	6CE	IR	1.904	ERLG97, REW90, REL00
6C0902+34	0902+343	09 02 24.77	+34 19 57.8	6CE	c, O, IR	3.395	COH94, L88, REL00
6C0905+39	0905+399	09 05 04.95	+39 55 34.9	6CE	c, IR	1.882	LGE95, REL00
3C217	0905+380	09 05 41.34	+38 00 29.9	3CRR	mc, HST	0.8975	BLR97, Lpc, RS97, SD84b
6C0919+38	0919+381	09 19 07.99	+38 06 52.5	6CE	IR	1.65 [#]	ER96, REL00
6C0930+38 [§]	0930+389	09 30 00.77	+38 55 09.1	6CE	h	2.395	NAR92, ER96, REL00
3C239	1008+467	10 08 38.98	+46 43 08.8	3CRR	mc, HST	1.781	Lpc, BLR97, MSvB95
MG1016+058	1016+058	10 16 56.82	+05 49 39.3	MG*	c, O, IR	2.765	DSD95
3C241	1019+222	10 19 09.38	+22 14 39.7	3CRR	CSS, HST	1.617	BLR97, SD84b
8C1039+68	1039+681	10 39 07.75	+68 06 06.6	8C*	O	2.53	Lthesis
6C1113+34	1113+349	11 13 47.64	+34 58 46.6	6CE	h, IR	2.406	LLA95, REL00
3C257	1120+057	11 20 34.55	+05 46 46.0	3C	O	2.474	Spriv, vBS98
3C265	1142+318	11 42 52.35	+31 50 26.6	3CRR	c, HST	0.8108	FBP97, BLR97, SJ79
3C266	1143+500	11 43 04.22	+50 02 47.4	3CRR	mc, HST	1.272	BLR97, LPR92, SD84b
3C267	1147+130	11 47 22.07	+13 03 60.0	3CRR	c, HST	1.144	BLR97, Lpc, SD84b
6C1159+36	1159+368	11 59 20.94	+36 51 36.2	6CE	CSS	3.2 [#]	NAR92, REL00
6C1204+37	1204+371	12 04 21.75	+37 08 20.0	6CE	IR	1.779	ERLG97, REL00
6C1232+39	1232+397	12 32 39.12	+39 42 09.4	6CE	c, IR	3.221	ERD93, NAR92, REW90, REL00
TX1243+036	1243+036	12 43 05.40	+03 39 44.5	TX*	c, O	3.57	vOR96 , RMC95, RvO97
MG1248+11	1248+113	12 48 29.11	+11 20 40.3	MG*	O	2.322	SDS99
3C277.2	1251+159	12 51 03.85	+15 58 47.1	3CRR	c, HST	0.766	Lpc, McC97, SDM85
4C24.28	1345+245	13 45 54.66	+24 30 44.7	4C*	O	2.879	CMvB96, RvO97
3C294	1404+344	14 04 34.06	+34 25 40.0	3CRR	c	1.786	MS90
8C1435+635	1435+635	14 35 27.50	+63 32 12.8	8C*	O	4.25	LMR94, SDG95
3C322	1533+557	15 33 46.27	+55 46 47.4	3CRR	mc	1.681	LRL, LLA95, SRS90
3C324	1547+215	15 47 37.14	+21 34 41.0	3CRR	c, HST, IR	1.2063	BCG98, BLR97, SD84a
3C340	1627+234	16 27 29.42	+23 26 42.2	3CRR	c	0.7754	Lpc, LRL, SD84b
53W002	1712+503	17 12 59.83	+50 18 51.3	LBDS	O	2.39	WBM91
53W069	1718+499	17 18 46.50	+49 47 47.7	LBDS	c, O	1.432	Wthesis, D99
3C356 [†] (a)	1732+510	17 23 06.77	+51 00 17.8	3CRR	c, IR	1.079	BLR97, S82
		17 23 06.95	+51 00 14.2	3CRR	c, IR		LR94
MG1744+18	1744+183	17 44 55.30	+18 22 11.3	MG*	IR	2.28 [‡]	Bthesis, S-unpub, ER93
4C13.66	1759+138	17 59 21.64	+13 51 22.8	3CRR	IR	1.45	RLL96
3C368	1802+110	18 02 45.63	+11 01 15.8	3CRR	c, HST	1.132	BLR97, DSP87, S82
4C40.36	1809+407	18 09 19.42	+40 44 38.9	4C*	O	2.265	CMvB88, RvO97
4C48.48	1931+480	19 31 40.03	+48 05 07.1	4C*	c, O	2.343	CMvB96, RvO97
4C23.56	2105+233	21 05 00.96	+23 19 37.7	4C*	c, O	2.483	CMvB96, RvO97
MG2141+192	2141+192	21 41 46.95	+19 15 26.7	MG*	h	3.592	CRvO97, Mprep,
3C437	2145+151	21 45 01.58	+15 06 36.1	3CRR	HST	1.48	BLR97, MSvB95
MG2305+03	2305+033	23 05 52.31	+03 20 47.9	MG*	O	2.457	SDS99
4C28.58	2349+288	23 49 26.94	+28 53 47.2	4C*	c, O	2.891	CMvB96, RvO97
3C470	2356+438	23 56 02.90	+43 48 03.6	3CRR	c, HST	1.653	Lpc, BLR97, MSvB95

array, optimised for an observing wavelength of 850 μm , contains 37 pixels. The short-wavelength (SW) array, optimised for operation at 450 μm , contains 91 pixels. A dichroic beamsplitter allows observations to be made with both arrays simultaneously.

For point sources, SCUBA's photometry mode is recommended, where the target is observed with a single pixel. During commissioning, it was discovered that the best photometric accuracy could be obtained by averaging the source signal over a slightly larger area than the beam. This is achieved by 'jiggle' the secondary mirror such that the chosen bolometer samples a 3×3 grid with 2" spacing centered on the source. The on-source integration time is 1 second per jiggle point; excluding overheads, the jiggle pattern takes 9 s to complete. While making the mini jiggle map, the telescope was chopped at 45" in azimuth at a frequency of 7Hz. After the first 9-point jiggle, the telescope was nodded to the reference position, an event which occurred every 18 seconds thereafter.

Between June 1997 and March 1999, a total of 192 hours was used to carry out the observations, all in excellent weather conditions. The atmospheric zenith opacities were at the very most 0.3 at 850 micron and 2.5 at 450 micron, although they were frequently much better than this. Skydips and observations of calibrators were obtained regularly. For each source, the data have been flatfielded, despiked, and averaged over 18 seconds. The residual sky background that chopping and nodding are unable to remove has been subtracted by using the data taken by the off-source bolometers. The Kolmogorov-Smirnov (KS) test has been applied to the data to check for consistency, and the data have been calibrated using observations of Mars, Uranus and several secondary calibrators.

The 850 μm and 450 μm flux densities measured for the radio galaxies in the sample are listed in Table 2. This table includes both 3σ upper limits for sources whose signal-to-noise ratio (S/N) does not exceed 3.0 and 2σ upper limits for sources whose S/N does not exceed 2.0. The reason for this is that while traditionally the detection of a given source might only be regarded as robust if it is greater than 3σ , genuine 2σ detections should be taken seriously, especially given that the telescope was pointed at known galaxies instead of the submillimetre source being identified in a blank-field survey. Furthermore, the adoption of a 2σ detection level is necessary to implement the statistical analysis presented in Section 7.1. It should be noted, however, that the results presented in this paper hold whether a 3σ or a 2σ detection threshold is adopted.

3.2 Radio galaxies with other millimetre/submillimetre observations

Several attempts were made to observe the millimetre/submillimetre spectrum of radio galaxies before SCUBA existed. The attempts, made with the IRAM 30-m telescope and UKT14 (SCUBA's predecessor), were largely unsuccessful. More recently, Best et al. (1998b) also looked at 3C324 with SCUBA and Benford et al. (1999) observed 4C41.17 at 350 μm with the CSO. All of these observations, including the full submillimetre spectrum of 8C1435+635, are listed in Table 3.

In most cases, these data are consistent with what we

observed with SCUBA (for 3C324, although we find a lower flux density than Best et al. (1998b), the two results are equivalent within errors). There are two exceptions:

(i) 53W002 - Even though 53W002 was detected at 800- μm with UKT14 (Hughes et al. 1997), we have failed to detect it with SCUBA. Assuming a typical submillimetre spectral index of -4.0 , the 800- μm detection of 53W002 implies a flux density of at least 3.6 mJy at 850- μm . Note the spectral index is expected to lie between the values of -3.0 and -4.0 (e.g. Hildebrand 1983), and adopting a value of -4.0 will give the lowest estimate of 850- μm flux. Thus, if the UKT14 data are trustworthy, we should have detected 53W002 with SCUBA, even if the large error bar on the 800- μm measurement is taken into account.

(ii) MG1016+058 - For MG1016+058, previous detections existed at both 1300 μm and 800 μm (Cimatti et al. 1998b). The minimum submillimetre spectral index consistent with these data points and their error bars is ~ -2.8 . This can be used to estimate a lower limit on the flux density expected at 850 μm . The 850- μm flux density should be well in excess of 5 mJy, easily detectable with SCUBA. An obvious objection to this analysis is that the 1300- μm flux density could be solely due to radio synchrotron emission. This is unlikely; the radio spectrum is highly curved and dives down well below the 1300- μm flux density (Appendix A). However, assume for a moment that the 1300- μm flux density was contaminated by radio emission. Again, adopting a typical submillimetre spectral index of -4.0 and applying it to the 800 μm detection still predicts an 850- μm flux density in excess of 5 mJy.

These two discrepancies are perhaps not all that surprising. UKT14 was a single-element bolometer, relying solely on chopping and nodding for sky removal. However, a chop/nod set-up is unable to account for quick variations in the background sky, and there will be residual sky noise present in the data (Jenness, Lightfoot & Holland 1998). SCUBA is an array, and the off-source bolometers can be used to remove this residual sky noise (Jenness et al. 1998). Omont et al. (1996) investigated the difference between single- and multi-bolometer detectors, and found that the less-reliable sky-cancellation offered by single-bolometer systems often resulted in fake detections of weak sources. Furthermore, they failed to detect three high-redshift quasars with a multi-bolometer array that Andreani, La Franca & Cristiani (1993) had apparently detected with a single bolometer.

4 CORRECTING RADIO GALAXY DUST EMISSION FOR POTENTIAL CONTAMINATION

For the majority of galaxies in the sample which we have actually detected, a detection has only been obtained at one submillimetre wavelength (i.e. 850 μm). Without a reliable estimate of the submillimetre spectral index, care needs to be taken to ensure the detected submillimetre emission is clearly in excess of the radio synchrotron spectrum, and can thus be safely attributed to dust. However, as will become clear, due to the fact that the sample was confined to steep-spectrum lobe-dominated radio galaxies at $z > 1$,

Table 2. Observed submillimetre flux densities (S_ν) and standard errors for the sample. 3σ upper limits are shown for sources whose S/N does not exceed 3.0; 2σ upper limits are shown for sources whose S/N does not exceed 2.0

Source	z	S_ν (mJy)	850 μm			S_ν (mJy)	450 μm		
			S/N	3σ limit (mJy)	2σ limit (mJy)		S/N	3σ limit (mJy)	2σ limit (mJy)
3C277.2	0.766	1.01 ± 1.04	1.0	< 4.13	< 3.09	-10.6 ± 10.7	-1.0	< 32	< 21
3C340	0.7754	0.85 ± 0.87	1.0	< 3.46	< 2.59	6.8 ± 9.0	0.8	< 34	< 25
3C265	0.8108	-1.41 ± 0.98	-1.4	< 2.94	< 1.96	-2.0 ± 11.2	-0.2	< 34	< 22
3C217	0.8975	1.03 ± 0.83	1.2	< 3.52	< 2.69	-0.7 ± 9.8	-0.1	< 30	< 20
3C356	1.079	1.66 ± 1.04	1.6	< 4.78	< 3.74	17.3 ± 19.8	0.9	< 77	< 57
3C368	1.132	4.08 ± 1.08	3.8			39.6 ± 15.1	2.6	< 85	
3C267	1.144	1.93 ± 0.96	2.0	< 4.81		27.0 ± 14.6	1.8	< 71	< 56
3C324	1.2063	1.75 ± 0.87	2.0	< 4.36		4.1 ± 11.8	0.3	< 39	< 28
3C266	1.272	0.46 ± 1.30	0.4	< 4.36	< 3.06	-2.1 ± 30.5	-0.1	< 91	< 61
53W069	1.432	-2.70 ± 1.04	-2.6	< 3.12	< 2.08	14.7 ± 11.5	1.3	< 49	< 38
4C13.66	1.45	3.53 ± 0.96	3.7			-16.2 ± 18.2	-0.9	< 55	< 36
3C437	1.48	-1.18 ± 0.98	-1.2	< 2.94	< 1.96	2.9 ± 17.3	0.2	< 55	< 37
3C241	1.617	1.81 ± 0.94	1.9	< 4.63	< 3.69	14.8 ± 12.6	1.2	< 52	< 40
6C0919+38	1.65	-0.88 ± 1.05	-0.8	< 3.15	< 2.10	10.5 ± 10.1	1.0	< 41	< 31
3C470	1.653	5.64 ± 1.08	5.2			57.8 ± 32.9	1.8	< 156	< 124
3C322	1.681	-0.05 ± 1.06	0.0	< 3.18	< 2.12	-37.5 ± 16.0	-2.3	< 48	< 32
6C1204+37	1.779	0.16 ± 1.25	0.1	< 3.91	< 2.66	45.1 ± 26.6	1.7	< 125	< 98
3C239	1.781	0.83 ± 1.00	0.8	< 3.83	< 2.83	-2.1 ± 18.3	-0.1	< 55	< 37
3C294	1.786	0.19 ± 0.78	0.2	< 2.53	< 1.75	5.4 ± 13.4	0.4	< 45	< 32
6C0820+36	1.86	2.07 ± 0.96	2.2	< 4.95		13.6 ± 18.0	0.8	< 68	< 50
6C0905+39	1.882	3.62 ± 0.89	4.1			31.2 ± 16.2	1.9	< 80	< 64
6C0901+35	1.904	-1.83 ± 1.15	-1.6	< 3.45	< 2.30	-19.3 ± 8.2	-2.4	< 25	< 16
5C7.269	2.218	1.68 ± 1.00	1.7	< 4.68	< 3.68	5.1 ± 9.2	0.6	< 33	< 23
4C40.36	2.265	0.67 ± 1.06	0.6	< 3.85	< 2.79	7.3 ± 23.2	0.3	< 77	< 54
MG1744+18	2.28	0.83 ± 1.02	0.8	< 3.89	< 2.87	13.2 ± 17.7	0.7	< 66	< 49
MG1248+11	2.322	1.10 ± 1.06	1.0	< 4.28	< 3.22	-20.9 ± 12.9	-1.6	< 39	< 26
4C48.48	2.343	5.05 ± 1.05	4.8			17.9 ± 24.9	0.7	< 93	< 68
53W002	2.39	1.03 ± 1.10	0.9	< 4.33	< 3.23	2.9 ± 14.3	0.2	< 46	< 32
6C0930+38	2.395	0.36 ± 1.00	0.4	< 3.36	< 2.36	8.3 ± 10.8	0.8	< 41	< 30
6C1113+34	2.406	0.33 ± 1.14	0.3	< 3.75	< 2.61	-11.4 ± 16.8	-0.7	< 50	< 34
MG2305+03	2.457	2.31 ± 0.99	2.3	< 5.28		-9.5 ± 41.8	-0.2	< 126	< 84
3C257	2.474	5.40 ± 0.95	5.7			17.8 ± 15.4	1.2	< 64	< 49
4C23.56	2.483	1.72 ± 0.98	1.8	< 4.66	< 3.68	-3.3 ± 17.0	-0.2	< 51	< 34
8C1039+68	2.53	0.38 ± 0.98	0.4	< 3.32	< 2.34	31.8 ± 17.0	1.9	< 83	< 66
MG1016+058	2.765	2.40 ± 0.92	2.6	< 5.16		28.7 ± 10.1	2.8	< 59	
4C24.28	2.879	2.59 ± 1.16	2.2	< 6.07		11.2 ± 18.7	0.6	< 67	< 48
4C28.58	2.891	3.93 ± 0.95	4.1			23.0 ± 15.5	1.5	< 69	< 54
6C1232+39	3.221	3.86 ± 0.72	5.4			-2.4 ± 6.1	-0.4	< 18	< 12
6C1159+36	3.2	1.20 ± 1.08	1.1	< 4.44	< 3.36	28.3 ± 16.0	1.8	< 76	< 60
6C0902+34	3.395	2.83 ± 1.00	2.8	< 5.83		11.6 ± 11.5	1.0	< 46	< 35
TX1243+036	3.57	2.28 ± 1.11	2.1	< 5.61		1.5 ± 19.0	0.1	< 59	< 40
MG2141+192	3.592	4.61 ± 0.96	4.8			21.4 ± 18.9	1.1	< 78	< 59
6C0032+412	3.66	2.64 ± 1.20	2.2	< 6.24		-5.5 ± 13.3	-0.4	< 40	< 27
4C60.07	3.788	17.11 ± 1.33	12.9			69.0 ± 23.0	3.0		
4C41.17	3.792	12.10 ± 0.88	13.8			22.5 ± 8.5	2.7	< 48	
8C1435+635	4.25	7.77 ± 0.76	10.2			23.6 ± 6.4	3.7		
6C0140+326	4.41	3.33 ± 1.49	2.2	< 7.80		-20.5 ± 17.1	-1.2	< 51	< 34

for almost all objects, detectability with SCUBA at 850 μm corresponds to a successful detection of dust. Radio spectra have been compiled for each source with the aim of extrapolating the radio emission to submillimetre wavelengths and subtracting it off. This correction should give a good estimate of the flux density produced by thermal dust emission.

It might appear that such a correction would be excessive, or even completely unnecessary where it is known that the radio lobes lie outside the SCUBA beam. However, at high frequencies, ≥ 8 GHz, experience with individual

well-studied objects (e.g. 4C41.17) indicates that much of the emission can arise from structures coincident or close to the radio core (e.g. Carilli, Owen & Harris 1994). Therefore we have adopted the conservative but consistent approach of estimating submillimetre synchrotron contamination from the extrapolation of the total high-frequency radio emission in every case. In practice, for radio sources larger than the JCMT beam, this correction makes a significant impact on the estimated dust mass in only a very small number of sources. These are discussed at the end of Section 4.1.

Table 3. All other millimetre and submillimetre observations of galaxies in the sample. All flux densities are quoted in mJy. The references are: 3C324 - BRB98; 53W002 - HDR97; 3C257 - HDR97; MG1016+058 - CFR98; 6C1232+39 - C&K94; 6C0902+34 - C&K94, DSS96, HDR97; TX1243+036 - CFR98; MG2141+192 - HDR97; 6C0032+412 - HDR97; 4C41.17 - BCO99, C&K94, DHR94; 8C1435+635 - HDR97, I95, IDHA98

Source	$S_{3000\mu m}$	$S_{1300\mu m}$	$S_{850\mu m}$	$S_{800\mu m}$	$S_{750\mu m}$	$S_{450\mu m}$	$S_{350\mu m}$	$S_{175\mu m}$
3C324			3.65 ± 1.17				$3\sigma < 21$	
53W002				6.9 ± 2.3				
3C257				$3\sigma < 11$				
MG1016+058		2.13 ± 0.47		14.7 ± 4.6				
6C1232+39		$3\sigma < 3.0$						
6C0902+34	4.2 ± 0.6	3.1 ± 0.6		$3\sigma < 14$				
TX1243+036		$3\sigma < 2.6$		$3\sigma < 9.3$				
MG2141+192				$3\sigma < 11$				
6C0032+412				$3\sigma < 14$				
4C41.17		2.5 ± 0.4		17.4 ± 3.1		$3\sigma < 56$	37 ± 9	
8C1435+643		2.57 ± 0.42	7.77 ± 0.76	$3\sigma < 13$	8.74 ± 3.31	23.6 ± 6.4	$3\sigma < 87.0$	$3\sigma < 40.1$

The radio spectra are shown in Appendix A, and include both integrated and core radio flux densities. Core flux densities are generally much fainter than the integrated radio emission at low frequencies, but they can also be much flatter. If the core has a flat spectral index, it may contribute significantly to the submillimetre flux density even if the integrated radio emission seems to fall well below this.

Fits to the radio spectra are also shown in Appendix A. These fits are described in Section 4.1 (with full details in Appendix A) and are subsequently used to estimate the non-thermal contamination at submillimetre wavelengths. Details on how the individual radio spectra were compiled are given in Archibald (1999).

Note the radio spectrum of 53W069 has not been presented here. 53W069 is only 3.73 mJy at 1.4 GHz, and synchrotron contamination will not be a problem (Windhorst et al. 1984).

4.1 Synchrotron contamination

A simple synchrotron spectrum is a power law of the form $S_\nu \propto \nu^{-\alpha}$. However, real radio spectra turn over at low frequencies owing to synchrotron self-absorption, or through running out of electrons at low energies. At high frequencies the spectra steepen as they age - the highest-energy electrons radiate away their energy the fastest. In log-space, such spectra appear curved.

Consider, as an example, the radio spectrum of the hotspots of Cygnus-A, described in detail by Muxlow, Pelletier & Roland (1988). The spectrum is a power law at low frequencies $0.4 \text{ GHz} < \nu < 1.5 \text{ GHz}$, with a spectral index $\alpha \sim 0.5$, and a low-frequency turn-over at $\nu \sim 0.2 \text{ GHz}$. At 2GHz the spectrum steepens; for $\nu > 2 \text{ GHz}$, the spectrum is consistent with a power law of index $\alpha \sim 1.0$. Robson et al. (1998) and Eales, Alexander & Duncan (1989) have found that this steep power law is an accurate description of the spectrum right out to submillimetre wavelengths. Thus in log-space, at high frequencies a straight-line fit would be accurate. However, when fitting to the whole spectrum, a model with some curvature would be required.

Another good example is the study of the dominant hotspot of 3C273, by Meisenheimer & Heavens (1986). For low frequencies, $\nu < 1.5 \text{ GHz}$, the spectral index is $\alpha \sim 0.7$.

For $1.5 \text{ GHz} < \nu < 5 \text{ GHz}$, the spectrum steepens to an index of $\alpha \sim 0.9$. At high frequencies $5 \text{ GHz} < \nu < 15 \text{ GHz}$, the spectrum steepens even further to an index of $\alpha \sim 1.0$.

More recently, Murgia et al. (1999) published a study of compact steep-spectrum radio sources. The majority of objects in their sample exhibit a clear spectral steepening, occurring anywhere from a few hundred MHz to tens of GHz.

In order to successfully correct for synchrotron contamination at submillimetre wavelengths, the high-frequency radio spectrum needs to be well determined. Unfortunately, for most galaxies in the sample, the highest-frequency observation is $\nu \sim 20 \text{ GHz}$. A straight-line extrapolation (in log-space) from the highest frequency data point could be used to decontaminate the submillimetre flux densities. However, in the interval between 20 GHz and the SCUBA wavebands, the spectrum may steepen, and the straight-line extrapolation would over-correct the SCUBA flux density.

Evidence to support this steepening comes from 3C324, MG1744+18, and MG1016+058 - the only sources in the sample with measured radio flux densities at $\nu > 20 \text{ GHz}$. In each case the high-frequency observation indicates a significant steepening of the radio spectrum. 4C23.56 and 8C1435+635, two of the higher-redshift galaxies in the sample, even appear significantly curved for $\nu < 20 \text{ GHz}$.

Note that if a straight-line extrapolation of the high-frequency radio emission is correct, three of 850- μm detections made with SCUBA appear to be seriously contaminated with non-thermal synchrotron - 4C13.66, 3C470, and 3C257.

More high-frequency radio observations are needed to be certain what the radio spectrum of each galaxy in the sample does as it approaches the submillimetre waveband. For now, both possibilities will be considered: a *linear fit*, a straight-line extrapolation of the high-frequency data, as could be accurately applied to Cygnus-A; and a *parabolic fit* which reflects a degree of steepening, or curvature, at higher frequencies. The details of the two fits, together with plots of the SEDs, are given in Appendix A.

It would be surprising if the radio spectra flattened off at high frequencies, as this only occurs if the source has an extremely bright, flat radio core (except for 6C0902+34, the radio galaxies discussed here all have relatively faint cores - Section 4.2). Thus, the linear fit is a strong upper limit

on the synchrotron emission at submillimetre wavelengths, especially since a significant fraction of the emission may lie outside the JCMT beam. Deviations from this standard power-law take the form of a steepening at high frequencies - the parabolic fit mimics this curvature and is a good lower limit on the amount of synchrotron emission at submillimetre wavelengths. Given the lack of high-frequency radio observations, it is often difficult to determine which is the better fit. The best estimate of the synchrotron contamination has been taken to be the midpoint of these two models, with the error in the estimate being the difference between the midpoint and either the upper or lower limit.

These estimates of synchrotron emission were thus subtracted from the measured SCUBA flux densities, with the errors being added in quadrature (as prescribed by the propagation of errors). However, there were four special cases for which particular care had to be taken:

(i) 3C324, MG1744+18, MG1016+058, and 4C23.56 all have high-frequency data that the linear fit has trouble fitting to. For these galaxies, the parabolic fit looks to be the more realistic extrapolation of the radio spectra, and was used to decontaminate the SCUBA flux densities.

(ii) For the 14 radio sources whose lobes lie outside the JCMT beam, we may have over-corrected for synchrotron contamination. However, for all of these but one, the source was either undetected by SCUBA, or the applied correction was insignificantly small. For 3C470, the applied correction turned a detection into a non-detection, reducing the 850 μm flux from 5.6 mJy to 3.1 mJy. However, as mentioned previously, our method of correction may be reasonable for sources that lie outside the JCMT beam. Furthermore, if the correction is not applied to 3C470, the results presented in the paper are unaffected.

(iii) For some galaxies SCUBA measured a negative signal. They have not been corrected for synchrotron contamination; performing the correction would have unnecessarily increased the noise of the measurement and inappropriately made the signal even more negative.

(iv) For some of the undetected galaxies, the estimated synchrotron contamination is larger than the signal measured by SCUBA, resulting in a negative submillimetre flux density if it is corrected for. Claiming a ‘negative emission’ from dust is not physically meaningful. It is better to set the SCUBA flux densities equal to zero: it appears that there is no thermal emission from dust at these wavelengths. This leaves the question of how to handle the errors. It seems best to leave them as they are - as they have been measured by SCUBA. The statement then being made is that, as far as it can be ascertained, all of the measured signal may be radio synchrotron emission, and any dust emission from the source is definitely less than $2\times$ the measured noise (for a 2σ upper limit). This seems a good, conservative upper limit - in each case the limit is larger than the original measured flux density.

4.2 Radio cores

When searching for thermal dust emission, the telescope is pointed at the optical/infrared ID of the galaxy. This position is coincident with the radio core (if one has been detected). A flat radio core could contribute at submillimetre

wavelengths. A useful exercise is to estimate the upper limit on this contribution for each source - if it tends to be negligible, the SCUBA flux densities will not need to be corrected.

Only 8 of the galaxies in the sample have their radio core detected at more than one frequency: 3C267, 3C324, 3C241, 4C23.56, 6C1232+39, 6C0902+34, TX1243+036, and 4C41.17. 6C0902+34 is a special case that is excluded from the following discussion; it will be treated separately at the end of this section. For the remaining 7 galaxies, the radio core spectral index has been estimated using the two highest-frequency core detections. 3C324 and 3C241 have relatively flat core spectra, with $\alpha \sim 0.35$. The majority, however, have very steep spectra, ranging from $\alpha \sim 0.7$ to $\alpha \sim 1.8$. Note that no detected core appears either completely flat or inverted (i.e. flux density *increasing* with frequency) between 1 GHz and 15 GHz. If these cores are extrapolated to submillimetre wavelengths, in all cases, save one, the core contribution is negligible: $< 0.05\text{mJy}$ at 850 μm . For 3C241, on the other hand, the core strength at 850 μm is likely to be $\sim 1\text{mJy}$.

For several galaxies in the sample, the radio core has been detected at a single frequency. Adopting the flattest measured spectral index of $\alpha \sim 0.35$, the corresponding core flux densities at 850 μm have been estimated. This is a pessimistic estimate, many of these galaxies may have steeper core spectra, but it is a good indication of the worst-case scenario. In all cases but three, the predicted core flux densities are negligible, $< 0.2\text{mJy}$. Higher 850 μm core flux densities are expected for 3C322 and 3C265. However, for these galaxies a negative signal was measured with SCUBA, and the core brightness is irrelevant. For MG1016+058, if the spectrum is flat, a core flux density of $\sim 0.8\text{mJy}$ is expected at 850 μm . If, on the other hand, the spectral index is steeper, $\alpha \sim 0.75$ for example, the core contamination is negligible.

A lack of sources with core detections at more than one frequency potentially hinders this analysis. However, given the available information it seems unlikely that the cores are significant except for 3C241 and MG1016+058. The core contribution in the case of 3C241 has been corrected for, as the core spectrum is definitely flat. For MG1016+058, on the other hand, it is impossible to know whether the core is flat or steep. Given this uncertainty, the SCUBA observations have not been corrected for core contamination. Instead, it is simply noted that MG1016+058 may have a large core contribution at submillimetre wavelengths.

It is mentioned in the literature that three galaxies have completely flat (or possibly inverted) cores at $\nu < 5$ GHz: 3C294 (MS90), 6C0905+39 (LGE95), and 6C0032+412 (BRE98; Jarvis et al., in preparation). These cores could contribute significantly to the observed SCUBA flux densities. However, Rudnick, Jones & Fiedler (1986) have studied flat cores in powerful radio galaxies. They found the cores often turned over or steepened at $\nu > 5$ GHz - a completely flat core at low frequencies does not mean that it will remain flat out to the submillimetre wavebands, indeed all evidence suggests it is very unlikely to do so.

In addition, note that for 3C356, two radio core identifications exist: one faint and steep, the other brighter and flat. Neither should significantly contribute at submillimetre wavelengths.

6C0919+38 could have a very bright radio core, \sim

6 mJy at 5 GHz. However, it is not clear whether the bright feature detected by Naundorf et al. (1992) is the radio core or a knot in the radio jet. Given the uncertainty, the possible radio core contamination is merely noted here and is not corrected for.

4.2.1 6C0902+34

6C0902+34 is a special case because of the brightness of its core, ~ 10 mJy, between 1.5 and 15 GHz. In addition, two slightly conflicting observations at 8 GHz make it difficult to be certain how steep the core spectrum is. If the flatter spectral index is used ($\alpha \sim 0.3$), the 3 mm and 1.3 mm detections of Downes et al. (1996) and Chini & Krügel (1994) look to be completely dominated by the radio core. Downes et al. (1996) came to the same conclusion, and predict the contribution of dust emission at 1.3 mm to be < 0.6 mJy. Even if the steeper spectral index is used ($\alpha \sim 1.0$), the detections could easily be dominated by the integrated radio spectrum (although higher-frequency radio detections are needed to confirm this).

When observed with SCUBA at 850 μ m, a 3σ upper limit of 5.83 mJy was measured. Combining this with Chini & Krügel's detection of 3.1 ± 0.6 mJy at 1300 μ m, the submillimetre spectral index is $|\alpha| \leq 2.0$. This is inconsistent with thermal dust emission being present, for which $|\alpha| > 2.0$. (Note that the submillimetre spectral indices are negative).

6C0902+34 appears completely dominated by radio synchrotron emission. It has thus been left out of the sample. Hereafter, we discuss a sample of 46 radio galaxies which excludes 6C0902+34.

4.3 Submillimetre confusion

4.3.1 Galactic cirrus confusion

Extrapolating the galactic cirrus confusion that *IRAS* measured at 100 μ m to 850 μ m at SCUBA resolution yields a cirrus confusion noise of $<< 1$ mJy beam $^{-1}$ in the direction of our targets. Thus, contamination by galactic cirrus should not be a problem for this study (see Hughes et al. 1997 and Helou & Beichman 1990 for detailed discussions).

4.3.2 Confusion by extragalactic sources

Hughes et al. (1998) performed the deepest submillimetre survey when they mapped the Hubble Deep Field with SCUBA. For 850 μ m, confusion was found to be a problem for sources weaker than 2 mJy. At the 2 mJy level, the source density of their map is ~ 1 source per 30 beams. In a large *blank-field* survey reaching 2 mJy, some detections will inevitably result from confusion, particularly if sources are strongly clustered. However, the chances that such false confusion-induced detections should coincide in position with known massive objects at high redshift is clearly extremely small. Of course, given sufficient resolution our detected sources may break up into sub-components, as for example has the optical image of 4C41.17 under HST resolution (Miley et al. 1992). However, since such sub-components are still extremely likely to be associated with

the radio galaxy itself, this cannot be regarded as a problem. See also Blain et al. (1998) for an in-depth discussion of source confusion at SCUBA wavelengths.

4.3.3 Confusion by sources in the off-beam

The measured flux densities could be affected by chopping onto a nearby source. This is unlikely to be an important problem for this study, even though SCUBA maps of the fields of radio galaxies have revealed an over-density of sources in some cases (Ivison et al. 2000a; Ivison et al., in preparation). For the galaxies in our sample which have been mapped and shown to have companion sources (4C41.17 and 8C1435+635), our chop did not land on the companions. Furthermore, our observations were made with an azimuthal chop, and the off-beam will have moved across a substantial angle (several degrees) of the sky as we tracked a source, diluting the effect of off-beam contamination. There is also no *a priori* reason why this possible source of confusion would result in a redshift bias and affect the analysis presented in Section 7.

4.4 A final note on corrections: 6C0140+326

As a final note on correcting the SCUBA flux densities, it appears that 6C0140+326 is gravitationally lensed (Rawlings et al. 1996a). However, the predicted amplification factor is small (< 2). Given the uncertainties in estimating this factor and the synchrotron contamination, a correction has not been applied.

4.5 Corrected flux densities

The final 850- μ m flux densities, corrected for synchrotron contamination, and in the case of 3C241 for radio core contamination, are presented in Table 4. Note, we do not include the corrected 450- μ m flux densities; at 450 μ m the corrections are tiny compared with the errors. As mentioned earlier, we adopt a detection threshold of $S/N \geq 2.0$, with upper limits taken at the 2σ level. Out of a sample of 46 radio galaxies (excluding 6C0902+34), thermal emission from dust has been detected in 14 galaxies at 850 μ m, and in 5 of these galaxies at 450 μ m.

For 3C368, MG1016+058, 4C60.07, 4C41.17, and 8C1435+635, an estimate of the 850-450 μ m spectral index can be made. For thermal dust emission, the slope along the Rayleigh-Jeans tail is expected to be around 3.0-4.0. The spectral indices of the lower- z detected sources, 3C368 and MG1016+058, are consistent with this: $|\alpha_{450}^{850}| \sim 4$. The indices of 4C60.07, 4C41.17 and 8C1435+635 are on the low side, $|\alpha_{450}^{850}| \leq 2$. However, this is to be expected. They have large redshifts, and for thermal greybody emission at 30 K, the spectral turnover should be redshifted into or near the 450 μ m waveband. Using the 450 μ m observation would underestimate the slope along the Rayleigh-Jeans tail in this situation.

Table 4. 850- μm flux densities (S_ν) and errors corrected for radio synchrotron contamination. In the case of 3C241, radio core contamination has also been taken into account. A ‘✓’ in column 2 indicates that applying the correction has changed the flux density by less than 1σ . 2σ upper limits are shown for sources whose S/N does not exceed 2.0.

Source	850 μm			
	$< 1\sigma$	S_ν (mJy)	S/N	2σ limit (mJy)
3C277.2	✓	0.00 ± 1.04	0.00	< 2.08
3C340	✓	0.00 ± 0.87	0.00	< 1.74
3C265	✓	-1.41 ± 0.98	-1.44	< 1.96
3C217		0.00 ± 0.83	0.00	< 1.66
3C356		0.08 ± 1.25	0.06	< 2.58
3C368	✓	3.70 ± 1.11	3.32	
3C267		0.00 ± 0.96	0.00	< 1.92
3C324		0.80 ± 0.89	0.90	< 2.57
3C266	✓	0.00 ± 1.30	0.00	< 2.60
53W069	✓	-2.70 ± 1.04	-2.60	< 2.08
4C13.66	✓	2.62 ± 1.24	2.11	
3C437	✓	-1.18 ± 0.98	-1.20	< 1.96
3C241		0.01 ± 1.15	0.00	< 2.30
6C0919+38	✓	-0.88 ± 1.05	-0.84	< 2.10
3C470		3.07 ± 1.56	1.96	< 6.20
3C322	✓	-0.05 ± 1.06	-0.05	< 2.12
6C1204+37	✓	0.00 ± 1.25	0.00	< 2.50
3C239	✓	0.00 ± 1.00	0.00	< 2.00
3C294	✓	0.00 ± 0.78	0.00	< 1.56
6C0820+36	✓	1.80 ± 0.98	1.83	< 3.76
6C0905+39	✓	3.52 ± 0.89	3.95	
6C0901+35	✓	-1.83 ± 1.15	-1.59	< 2.30
5C7.269	✓	1.41 ± 1.00	1.41	< 3.41
4C40.36	✓	0.63 ± 1.06	0.60	< 2.75
MG1744+18	✓	0.02 ± 1.02	0.02	< 2.06
MG1248+11	✓	0.96 ± 1.07	0.90	< 3.10
4C48.48	✓	4.72 ± 1.06	4.44	
53W002	✓	0.99 ± 1.10	0.90	< 3.19
6C0930+38	✓	0.00 ± 1.00	0.00	< 2.00
6C1113+34	✓	0.00 ± 1.14	0.00	< 2.28
MG2305+03		0.08 ± 1.02	0.08	< 2.13
3C257		1.62 ± 2.25	0.72	< 6.12
4C23.56	✓	1.68 ± 0.98	1.72	< 3.64
8C1039+68	✓	0.02 ± 0.99	0.02	< 2.01
MG1016+058	✓	2.31 ± 0.92	2.51	
4C24.28	✓	2.35 ± 1.17	2.01	
4C28.58	✓	3.89 ± 0.95	4.10	
6C1232+39	✓	3.84 ± 0.72	5.34	
6C1159+36	✓	0.79 ± 1.15	0.68	< 3.09
TX1243+036	✓	2.14 ± 1.11	1.92	< 4.36
MG2141+192	✓	4.57 ± 0.96	4.75	
6C0032+412	✓	2.40 ± 1.20	2.00	
4C60.07	✓	17.08 ± 1.33	12.84	
4C41.17	✓	12.06 ± 0.88	13.70	
8C1435+635	✓	7.76 ± 0.76	10.21	
6C0140+326	✓	3.31 ± 1.49	2.22	

5 THE RADIO LUMINOSITY-REDSHIFT PLANE FOR RADIO GALAXIES OBSERVED WITH SCUBA

It is useful to plot radio luminosity against redshift (the P-z plane) highlighting the galaxies we have observed with SCUBA. This ensures that even luminosity coverage of the P-z plane has been achieved, and identifies the redshifts

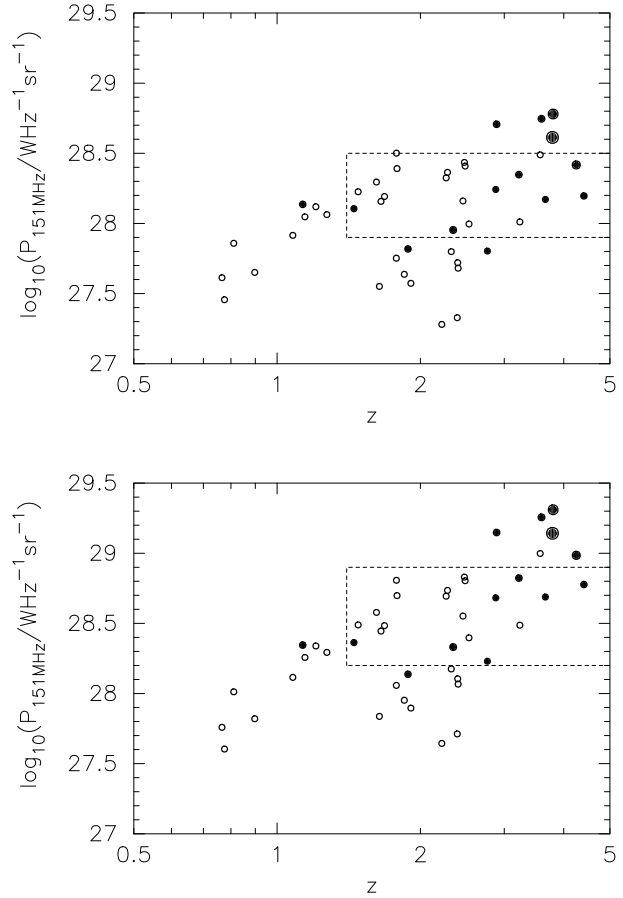


Figure 2. Radio luminosity-redshift plane for $\Omega_0 = 1.0$ (upper plot) and $\Omega_0 = 0.1$ (lower plot), assuming $H_0 = 50 \text{ kms}^{-1} \text{Mpc}^{-1}$. The solid circles indicate radio galaxies for which thermal emission from dust was detected at 850 μm with $S/N > 2$, and the open circles indicate galaxies for which no dust emission was detected. For the detections, the size of the solid circle represents the brightness of the galaxy at 850 μm . The 151-MHz radio luminosities, $P_{151\text{MHz}}$, were estimated using the radio SEDs presented and referenced in Appendix A. Note, 53W069 is too faint to appear on this version of the radio luminosity-redshift plane. The dashed-line boxes depict Subset A (upper plot) and Subset B (lower plot) which are defined in Section 7.1.

at which submillimetre emission from radio galaxies is detected.

As previously mentioned, the radio luminosities have been calculated at rest-frame 151 MHz to ensure that the radio luminosity tracks the power of the radio jets as accurately as possible. Simple physical models for the time development of the 151 MHz luminosity and the linear size (D_{linear}) of a double radio source suggest that over a large range of D_{linear} , the 151 MHz radio luminosity gives a reasonably accurate guide to the jet power Q of the vast majority of objects detected in complete radio flux-limited samples (Willott et al. 1999).

Both the 151 MHz luminosities and the linear sizes for the sample have been calculated for two cosmologies: $\Omega_0 = 1.0$, and $\Omega_0 = 0.1$, where $H_0 = 50 \text{ kms}^{-1} \text{Mpc}^{-1}$. The values are presented in Table 5. Figure 2 shows the corresponding P-z plane for each cosmology.

A proper statistical analysis of these data will be presented in Section 7, but at first glance, Figure 2 seems to indicate that submillimetre emission is more predominant in high-redshift radio galaxies than in low-redshift radio galaxies.

6 SUBMILLIMETRE LUMINOSITIES AND DUST MASSES

To calculate the rest-frame 850- μm luminosity ($L_{850\mu\text{m}}$) and dust mass (M_{dust}) of each source, we adopt an optically thin isothermal dust emission template with $\beta = 1.5$ and $T_{\text{dust}} = 40$ K. This template is consistent with the studies attempting to constrain β and T_{dust} that have been published in the literature. For example, Benford et al. (1999) have observed a sample of high-redshift radio-quiet quasars and radio galaxies at 350- μm . Assuming a critical wavelength of $\lambda_c = 125\mu\text{m}$, isothermal fits indicate $\beta \sim 1.5$ and $T_{\text{dust}} \sim 50$ K. The study of *IRAS* galaxies by Dunne et al. (2000) indicates $\beta \sim 1.2$ and $T_{\text{dust}} \sim 36$ K (although the value β is thought to have been artificially lowered by the presence of a cold dust component). Finally, for the handful of galaxies identified in the recent SCUBA surveys that have known redshifts (refer to Smail et al. 2000 for a review), the favoured value of T_{dust} is ~ 40 K (e.g. Ivison et al. 1998b, 2000b; Barger, Cowie & Sanders 1999).

It is currently impossible to determine the precise values of β and T_{dust} , and even though we have assumed the most likely template, it could very well be wrong. This has important consequences for the analysis presented here. For greybody emission, the values of β and T_{dust} determine the shape and position of the spectral turnover, but have less of an effect on the Rayleigh-Jeans tail. As the redshift of the source increases, the spectral peak is brought into view. Thus the K-correction used to calculate the 850- μm luminosity is more sensitive to changing the values of β and T_{dust} at high redshift than it is at low redshift. If the template is wrong, the error in the estimations of $L_{850\mu\text{m}}$ will be larger if the source has a high redshift. To explore this, the analysis of evolutionary trends has been conducted using several β - T_{dust} combinations, in addition to the template itself, to ensure the trends are real.

Furthermore, applying a template to the entire sample assumes that the individual radio galaxies all have similar dust parameters. This is a reasonable assumption if the same mechanisms for creating and heating dust are expected in each source. If, however, the dust characteristics do vary from source to source, they would have to do so in a redshift- (or radio power-) dependent manner to seriously affect the evolutionary trends presented here.

The choice of cosmology is also an important issue. As the relative properties of the sample are of most interest in the analysis presented here, the value of the Hubble constant is irrelevant. Changing the Hubble constant simply scales all the luminosities up or down by the same amount. However, changing the value of the density parameter affects the luminosities in a redshift-dependent manner. In order to encompass all possibilities, we thus consider two extreme values: $\Omega_o = 1.0$ and $\Omega_o = 0.1$, with $H_o = 50 \text{ km s}^{-1} \text{Mpc}^{-1}$. In Section 7.2 a low-density Universe ($\Omega_o = 0.1$) with $H_o = 67$ is also considered. The reason for this last choice is that the

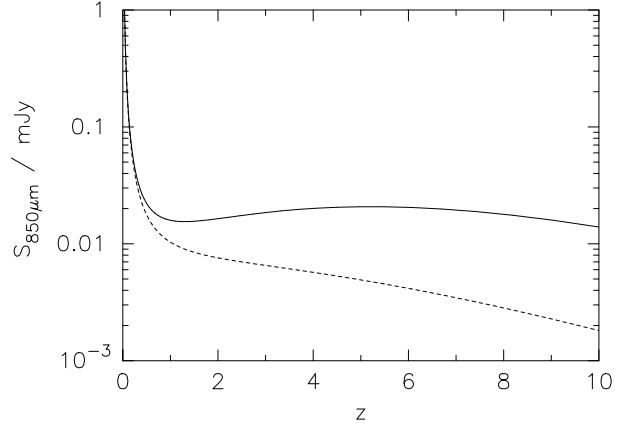


Figure 3. The 850 μm flux density that would be observed for the starburst galaxy M82 (Hughes, Gear & Robson 1994) if it were placed at progressively higher redshifts, assuming the dust emission template adopted here ($\beta = 1.5$, $T = 40$ K). The solid line represents an $\Omega_o = 1.0$ Universe; the dashed line represents an $\Omega_o = 0.1$ Universe ($H_o = 50 \text{ km}^{-1} \text{Mpc}^{-1}$).

age of a Universe with $\Omega_o = 1.0$, $H_o = 50$, is ~ 13 Gyr. A Universe with $\Omega_o = 0.1$, $H_o = 67$ has the same age - hence the ‘absolute values’ of the luminosities in these high and low density cases can be realistically compared. Recall the cosmological constant, Λ , is assumed to be zero throughout. It is worth noting that the evidence from the Supernova Cosmology Project is currently in favour of a cosmology with $\Omega_M = 0.3$ and $\Omega_\Lambda = 0.7$ (e.g. Perlmutter et al. 1999). This cosmology produces intermediate results to the two cosmologies considered here.

6.1 Implication of the adopted template

It is worth investigating what happens to the 850- μm flux density of M82 as it is placed at progressively higher redshifts, assuming the chosen dust template of $\beta = 1.5$ and $T_{\text{dust}} = 40$ K.

Figure 3 demonstrates that in an $\Omega_o = 1.0$ Universe, the 850- μm flux density is almost flat between $z = 1$ and $z = 4$; the 850- μm flux density should effectively trace the 850- μm luminosity.

In an $\Omega_o = 0.1$ Universe, on the other hand, SCUBA is less sensitive to $z = 4$ galaxies than it is to those at $z = 1$. Thus, the higher redshift objects in the sample should be more luminous than those at lower redshifts if they are detected at the same level.

The act of increasing β and T_{dust} will effectively make SCUBA more sensitive to submillimetre emission at $z = 4$ than $z = 1$. For a given set of fluxes, the luminosities at $z = 4$ will be reduced relative to those at $z = 1$ if β and T_{dust} are increased. Likewise, decreasing β and T_{dust} increases the inferred 850- μm luminosities at $z = 4$ relative to those at $z = 1$.

6.2 $L_{850\mu\text{m}}$ for the radio galaxy sample

Table 6 gives the 850- μm luminosities and dust masses for the radio galaxy sample. The optically thin, isothermal tem-

Table 5. Radio sizes and luminosities for the sample. Column 3 gives the largest angular size (LAS) of the radio source, measured in arcseconds. The corresponding linear size (D_{linear}) and 151-MHz radio luminosity ($P_{151\text{MHz}}$) have been calculated for both $\Omega_o = 1.0$ and $\Omega_o = 0.1$ ($H_o = 50 \text{ km s}^{-1} \text{Mpc}^{-1}$). The radio luminosities were estimated using the radio spectral energy distributions presented and referenced in Appendix A. The references for the LAS values are given in column 8. Where necessary, the LAS was measured off published radio maps. For the majority of the 3CRR sources, the LAS was taken from Blundell et al. (2000), which summarises the radio properties of these sources.

Source	z	LAS ($''$)	$\Omega_o = 1.0$		$\Omega_o = 0.1$		Refs.
			D_{linear} (kpc)	$\log P_{151\text{MHz}}$ ($\text{WHz}^{-1}\text{sr}^{-1}$)	D_{linear} (kpc)	$\log P_{151\text{MHz}}$ ($\text{WHz}^{-1}\text{sr}^{-1}$)	
3C277.2	0.766	58.0	473	27.61	559	27.76	BRR00
3C340	0.7754	46.7	382	27.46	452	27.60	BRR00
3C265	0.8108	78.0	643	27.86	768	28.01	BRR00
3C217	0.8975	12.0	101	27.65	122	27.82	BRR00
3C356	1.079	75.0	643	27.92	809	28.12	BRR00
3C368	1.132	7.9	68	28.14	86	28.35	BRR00
3C267	1.144	38.0	327	28.05	416	28.26	BRR00
3C324	1.2063	10.0	86	28.12	111	28.34	BRR00
3C266	1.272	4.5	39	28.06	51	28.29	BRR00
53W069	1.432	< 5.1	< 44	24.54	< 59	24.80	WvHK84
4C13.66	1.45	6.0	51	28.11	69	28.36	BRR00
3C437	1.48	34.4	294	28.23	398	28.49	BRR00
3C241	1.617	0.9	8	28.30	11	28.58	BRR00
6C0919+38	1.65	10.4	88	27.55	122	27.84	NAR92
3C470	1.653	24.0	203	28.16	283	28.45	BRR00
3C322	1.681	33.0	279	28.19	390	28.48	BRR00
6C1204+37	1.779	51.7	433	27.75	615	28.06	LLA95
3C239	1.781	11.2	94	28.50	133	28.81	BRR00
3C294	1.786	15.0	125	28.39	179	28.70	BRR00
6C0820+36	1.86	23.0	191	27.64	275	27.95	LLA95
6C0905+39	1.882	111.0	920	27.82	1330	28.14	LGE95
6C0901+35	1.904	2.7	22	27.57	32	27.90	NAR92
5C7.269	2.218	7.7	62	27.28	94	27.64	BRR00
4C40.36	2.265	4.0	32	28.33	49	28.69	CRvO97
MG1744+18	2.28	7.5	60	28.36	91	28.74	CRvO97
MG1248+11	2.322	< 1.2	< 9	27.80	< 15	28.18	LBH86
4C48.48	2.343	14.0	110	27.95	171	28.33	CRvO97
53W002	2.39	0.7	5	27.33	9	27.71	WBM91
6C0930+38	2.395	3.7	29	27.72	45	28.11	NAR92
6C1113+34	2.406	16.5	129	27.68	201	28.07	LLA95
MG2305+03	2.457	3.0	23	28.16	37	28.55	SDS99
3C257	2.474	12.0	93	28.44	147	28.83	vBS98
4C23.56	2.483	53.0	411	28.41	647	28.80	CRvO97
8C1039+68	2.53	15.0	116	28.00	183	28.40	Lthesis
MG1016+058	2.765	1.3	10	27.80	16	28.23	DSD95
4C24.28	2.879	2.3	17	28.24	28	28.68	CRvO97
4C28.58	2.891	16.2	119	28.71	198	29.15	CMvB96
6C1232+39	3.221	7.7	54	28.35	94	28.82	NAR92
6C1159+36	3.2	1.2	8	28.01	15	28.49	LLA95
TX1243+036	3.57	8.8	60	28.49	107	29.00	vOR96
MG2141+192	3.592	8.9	60	28.75	108	29.26	CRvO97
6C0032+412	3.66	2.3	15	28.17	28	28.69	BRE98
4C60.07	3.788	9.0	59	28.61	109	29.14	CRvO97
4C41.17	3.792	13.1	86	28.78	159	29.31	COH94
8C1435+635	4.25	3.9	24	28.42	47	28.99	LMR94
6C0140+326	4.41	2.5	15	28.20	30	28.78	RLB96, BRE98

plate spectrum with $\beta = 1.5$ and $T_{dust} = 40\text{K}$ has been assumed. The errors on the values of $L_{850\mu\text{m}}$ and M_{dust} have been calculated using the errors in the flux density measurements only; they do not account for the uncertainties in cosmology, β , or T_{dust} .

The dust mass of each galaxy in the sample was calculated from the 850- μm observation using:

$$M_{dust} = \frac{S_{obs} D_L^2}{(1+z) \kappa_{\nu_{rest}} B_{\nu_{rest}}(T_{dust})} \quad (1)$$

where S_{obs} is the observed flux-density, ν_{rest} is the corresponding rest-frame frequency, D_L is the luminosity distance to the source, $\kappa_{\nu_{rest}}$ is the mass absorption coefficient of the dust at ν_{rest} , and $B_{\nu_{rest}}(T_{dust})$ is the intensity of a blackbody at ν_{rest} assuming isothermal emission from

dust grains at a temperature T_{dust} . The mass absorption coefficient κ is poorly constrained, with published values of $\kappa(800\mu\text{m})$: $0.04 \text{ m}^2\text{kg}^{-1}$ (Draine & Lee 1984), $0.12 \text{ m}^2\text{kg}^{-1}$ (Chini, Krügel, & Kreysa 1986), $0.15 \text{ m}^2\text{kg}^{-1}$ (Hildebrand 1983), and $0.3 \text{ m}^2\text{kg}^{-1}$ (Mathis & Whiffen 1989). These estimates can be extrapolated to other wavelengths using $\kappa \propto \lambda^{-\beta}$ (Chini et al. 1986). The intermediate value of $\kappa(800\mu\text{m})=0.15 \text{ m}^2\text{kg}^{-1}$ will be assumed here. A different choice will not affect the relative dust masses of the sample, and can only alter the absolute dust masses by a factor of ~ 4 at most (Hughes et al. 1997).

In Figure 4, the $850\text{-}\mu\text{m}$ flux density is plotted against redshift for the radio galaxy sample. Plots of $L_{850\mu\text{m}}$ vs. z in $\Omega_0 = 1.0$ and $\Omega_0 = 0.1$ Universes are also shown. As expected from Figure 3, in the $\Omega_0 = 1.0$ case the flux density traces the luminosity between $z = 1$ and $z = 4$, and the two plots look the same. For $\Omega_0 = 0.1$, the luminosity of the $z \sim 4$ galaxies is higher relative to those at $z \sim 1$, as SCUBA is less sensitive to the high-redshift objects.

The small dynamic range in the measured values of $L_{850\mu\text{m}}$ for this study are limited by the sensitivity of SCUBA and the characteristic dust mass in high-redshift objects. Note the detections of $L_{850\mu\text{m}}$ appear at roughly the same level as the $L_{850\mu\text{m}}$ upper limits; most of the galaxies in the sample have been observed to the same depth in $850\text{-}\mu\text{m}$ *luminosity*. Coupled with the fact that the upper limits are clustered at the low-redshift end of the sample, this indicates that the high-redshift radio galaxies are intrinsically brighter in the submillimetre than the lower-redshift radio galaxies. This evidence for evolution of the radio galaxy population with redshift will now be analysed in detail.

7 EVIDENCE FOR EVOLUTION

7.1 Survival analysis: correlations between radio properties, submillimetre properties, and redshift

A logical approach to finding evidence which either supports or rejects the evolution scenario is to run correlation tests between the radio properties, submillimetre properties, and redshifts of the sample. For example, a correlation between $L_{850\mu\text{m}}$ and redshift, in the absence of a correlation between $L_{850\mu\text{m}}$ and $P_{151\text{MHz}}$, will imply that radio galaxies undergo cosmological evolution of their submillimetre emission. Conversely, a significant correlation between $L_{850\mu\text{m}}$ and $P_{151\text{MHz}}$ in the absence of a correlation between $L_{850\mu\text{m}}$ and redshift, would indicate that the submillimetre properties of radio galaxies are more closely tied to the radio properties of the galaxy (perhaps, for example, via host mass) than to cosmological epoch.

The obvious correlations to consider are between $L_{850\mu\text{m}}$, $P_{151\text{MHz}}$, and z . It is also instructive to investigate whether $P_{151\text{MHz}}$ correlates with D_{linear} (the linear size of the radio source), and whether the radio spectral index α_{radio} correlates with either $L_{850\mu\text{m}}$, $P_{151\text{MHz}}$, or z .

As mentioned previously, for radio sources selected from flux-limited samples, the 151-MHz radio luminosity should be a good indicator of the intrinsic power Q of the radio jet. The size of a radio source depends on its age, the medium it is expanding into, and the jet power. Again, considering sources from flux-limited samples, Willott et al. (1999)

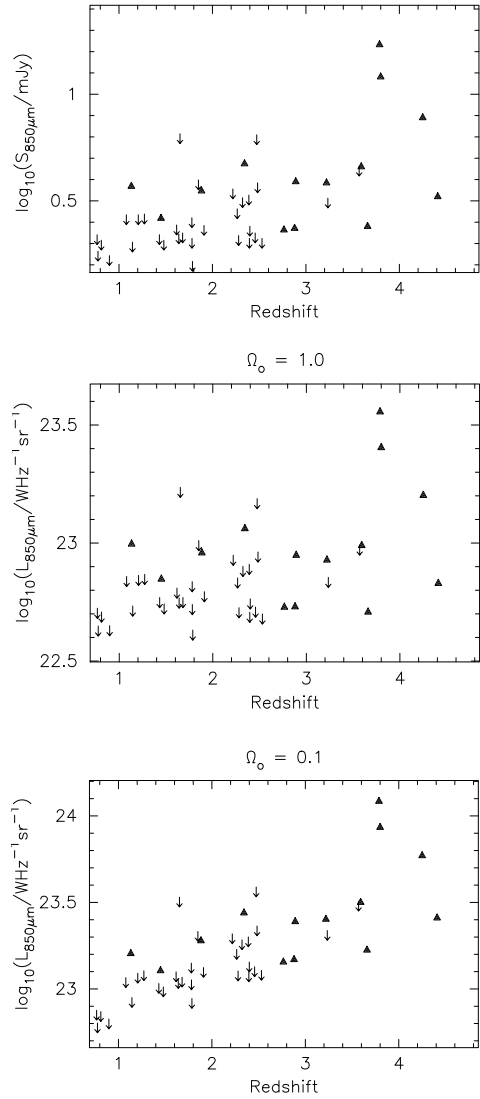


Figure 4. Scatter plots of $850\text{-}\mu\text{m}$ flux density and (rest-frame) luminosity against redshift for the radio galaxy sample. $L_{850\mu\text{m}}$ has been calculated assuming $\beta = 1.5$ and $T_{dust} = 40\text{K}$, and is shown for both $\Omega_0 = 1.0$ and $\Omega_0 = 0.1$ (H_0 is assumed to be $50 \text{ kms}^{-1}\text{Mpc}^{-1}$).

showed that the dependence of D_{linear} on jet power is very weak; D_{linear} correlates most strongly with the age of the radio source. Although radio luminosities are expected to decline throughout the lifetime of radio sources (Kaiser, Dennett-Thorpe & Alexander 1997; Blundell et al. 1999; Blundell & Rawlings 1999), selection effects conspire to ensure a very weak anti-correlation of radio luminosity with D_{linear} for sources selected from a number of separate flux-limited samples (Blundell et al. 1999). Although our sample of SCUBA targets is not purely a combination of flux-limited samples, it is dominated by 3C/3CRR and 6CE targets so no strong $P_{151\text{MHz}}\text{-}D$ links are expected.

The criterion that α_{radio} is large is often used to identify high redshift sources in large radio surveys. This selection is based on the empirical correlation observed between α_{radio} and radio luminosity (e.g. Veron, Veron & Witzel 1972). In

Table 6. Rest-frame 850- μ m luminosities ($L_{850\mu m}$) and dust masses (M_{dust}) for the radio galaxy sample. Optically thin, isothermal greybody emission has been assumed, with $\beta = 1.5$ and $T_{dust} = 40$ K. Errors have been estimated using only the standard errors on the flux density measurements; 2σ upper limits are given for undetected ($S/N < 2$) sources. $L_{850\mu m}$ and M_{dust} have been calculated for three different cosmologies: $\Omega_o=1.0$, $H_o=50$ kms $^{-1}$ Mpc $^{-1}$; $\Omega_o=0.1$, $H_o=50$ kms $^{-1}$ Mpc $^{-1}$; $\Omega_o=0.1$, $H_o=67$ kms $^{-1}$ Mpc $^{-1}$. Note, column 3 indicates whether the source belongs to either or the subsets defined in Section 7.1.

Source	z	Subset	$\Omega_o=1.0$, $H_o=50$		$\Omega_o=0.1$, $H_o=50$		$\Omega_o=0.1$, $H_o=67$	
			$\log L_{850\mu m}$ (WHz $^{-1}$ sr $^{-1}$)	$\log M_{dust}$ (M $_{\odot}$)	$\log L_{850\mu m}$ (WHz $^{-1}$ sr $^{-1}$)	$\log M_{dust}$ (M $_{\odot}$)	$\log L_{850\mu m}$ (WHz $^{-1}$ sr $^{-1}$)	$\log M_{dust}$ (M $_{\odot}$)
3C277.2	0.766		< 22.70	< 8.18	< 22.85	< 8.32	< 22.59	< 8.07
3C340	0.775		< 22.63	< 8.10	< 22.77	< 8.25	< 22.52	< 8.00
3C265	0.811		< 22.69	< 8.16	< 22.84	< 8.32	< 22.59	< 8.06
3C217	0.897		< 22.63	< 8.10	< 22.80	< 8.27	< 22.54	< 8.02
3C356	1.079		< 22.84	< 8.31	< 23.04	< 8.51	< 22.78	< 8.26
3C368	1.132		23.00	8.47	23.20	8.68	22.95	8.43
3C267	1.144		< 22.71	< 8.19	< 22.92	< 8.40	< 22.67	< 8.14
3C324	1.206		< 22.84	< 8.32	< 23.06	< 8.54	< 22.81	< 8.28
3C266	1.272		< 22.85	< 8.32	< 23.08	< 8.55	< 22.82	< 8.30
53W069	1.432		< 22.75	< 8.22	< 23.00	< 8.48	< 22.75	< 8.22
4C13.66	1.45	A,B	22.85	8.32	23.11	8.58	22.85	8.33
3C437	1.48	A,B	< 22.72	< 8.20	< 22.98	< 8.46	< 22.73	< 8.20
3C241	1.617	A,B	< 22.79	< 8.26	< 23.07	< 8.55	< 22.82	< 8.29
6C0919+38	1.65		< 22.75	< 8.22	< 23.03	< 8.51	< 22.78	< 8.25
3C470	1.653	A,B	< 23.21	< 8.69	< 23.50	< 8.98	< 23.25	< 8.72
3C322	1.681	A,B	< 22.75	< 8.22	< 23.04	< 8.52	< 22.79	< 8.26
6C1204+37	1.779		< 22.81	< 8.29	< 23.12	< 8.60	< 22.87	< 8.34
3C239	1.781	A,B	< 22.72	< 8.19	< 23.02	< 8.50	< 22.77	< 8.25
3C294	1.786	A,B	< 22.61	< 8.09	< 22.92	< 8.39	< 22.66	< 8.14
6C0820+36	1.86		< 22.99	< 8.46	< 23.30	< 8.78	< 23.05	< 8.53
6C0905+39	1.882		22.96	8.43	23.28	8.75	23.02	8.50
6C0901+35	1.904		< 22.77	< 8.25	< 23.10	< 8.57	< 22.84	< 8.32
5C7.269	2.218		< 22.93	< 8.40	< 23.29	< 8.77	< 23.04	< 8.51
4C40.36	2.265	A,B	< 22.83	< 8.31	< 23.20	< 8.68	< 22.95	< 8.42
MG1744+18	2.28	A,B	< 22.70	< 8.18	< 23.08	< 8.55	< 22.82	< 8.30
MG1248+11	2.322		< 22.88	< 8.36	< 23.26	< 8.73	< 23.00	< 8.48
4C48.48	2.343	A,B	23.06	8.54	23.44	8.92	23.19	8.66
53W002	2.39		< 22.89	< 8.36	< 23.27	< 8.75	< 23.02	< 8.49
6C0930+38	2.395		< 22.69	< 8.16	< 23.07	< 8.55	< 22.82	< 8.29
6C1113+34	2.406		< 22.74	< 8.22	< 23.13	< 8.60	< 22.87	< 8.35
MG2305+03	2.457	A,B	< 22.71	< 8.18	< 23.10	< 8.57	< 22.84	< 8.32
3C257	2.474	A,B	< 23.17	< 8.64	< 23.56	< 9.04	< 23.31	< 8.78
4C23.56	2.483	A,B	< 22.94	< 8.42	< 23.34	< 8.81	< 23.08	< 8.56
8C1039+68	2.53	A,B	< 22.68	< 8.15	< 23.08	< 8.55	< 22.82	< 8.30
MG1016+058	2.765	B	22.73	8.20	23.16	8.63	22.90	8.38
4C24.28	2.879	A,B	22.73	8.21	23.17	8.65	22.92	8.39
4C28.58	2.891		22.95	8.42	23.39	8.86	23.13	8.61
6C1232+39	3.221	A,B	22.93	8.40	23.40	8.88	23.15	8.62
6C1159+36	3.2	A,B	< 22.83	< 8.31	< 23.31	< 8.78	< 23.06	< 8.53
TX1243+036	3.57	A	< 22.97	< 8.45	< 23.48	< 8.95	< 23.22	< 8.70
MG2141+192	3.592		22.99	8.47	23.50	8.98	23.25	8.72
6C0032+412	3.66	A,B	22.71	8.18	23.22	8.70	22.97	8.45
4C60.07	3.788		23.56	9.03	24.08	9.56	23.83	9.31
4C41.17	3.792		23.40	8.88	23.93	9.41	23.68	9.16
8C1435+635	4.25	A	23.20	8.68	23.77	9.25	23.52	8.99
6C0140+326	4.41	A,B	22.83	8.30	23.41	8.89	23.16	8.63

a flux-limited survey, high values of α_{radio} will often correspond to a large intrinsic luminosity and hence to a high redshift.

However, it is possible to envisage models in which α_{radio} is related closely to star-formation activity (e.g. Lilly 1989). This is relevant to the work presented here, as several of the high-redshift galaxies in the sample were originally identified in these ultra-steep spectrum searches (e.g.

Chambers, Miley & van Breugel 1988, 1990; Chambers et al. 1996; Stern et al. 1999). Thus, if $L_{850\mu m}$ appears correlated with redshift, it could be a manifestation of how the sources were selected in the first place, a possibility which can be tested by investigating whether a correlation exists between $L_{850\mu m}$ and α_{radio} . Note, for the correlation analysis, α_{radio} was calculated at 151 MHz.

Table 7. Results of the survival analysis correlation tests applied to the entire sample. The significance (P) is the probability of the null hypothesis (*no correlation*) being true. If all three tests yield $P \leq 5$ per cent, the variables are taken to be correlated. If only some of the tests yield $P \leq 5$ per cent, evidence for a correlation is taken to be uncertain.

Cosmology	Variable Dependent	Variable Independent	Percentage of Data Censored	Significance (P)			Correlation Present?
				Cox	Kendall	Spearman	
–	$S_{850\mu m}$	z	70%	0.00%	0.02%	0.01%	YES
$\Omega_o = 1.0$	D_{linear}	$\log(P_{151MHz})$	4%	22.48%	82.69%	71.17%	NO
	$\log(P_{151MHz})$	z	0%	0.01%	0.03%	0.07%	YES
	$\log(L_{850\mu m})$	$\log(P_{151MHz})$	70%	2.65%	0.21%	0.64%	YES
	$\log(L_{850\mu m})$	z	70%	0.00%	0.19%	0.08%	YES
	$\log(L_{850\mu m})$	α_{radio}	70%	0.31%	0.36%	1.73%	YES
	α_{radio}	$\log(P_{151MHz})$	0%	0.64%	1.00%	1.36%	YES
$\Omega_o = 0.1$	α_{radio}	z	0%	4.18%	13.94%	10.50%	MAYBE
	D_{linear}	$\log(P_{151MHz})$	4%	32.29%	67.59%	50.22%	NO
	$\log(P_{151MHz})$	z	0%	0.00%	0.00%	0.00%	YES
	$\log(L_{850\mu m})$	$\log(P_{151MHz})$	70%	0.53%	0.01%	0.08%	YES
	$\log(L_{850\mu m})$	z	70%	0.00%	0.00%	0.00%	YES
	$\log(L_{850\mu m})$	α_{radio}	70%	0.18%	0.67%	1.88%	YES
Total Number of Galaxies: 46							

7.1.1 Survival analysis

The submillimetre dataset for the radio galaxy sample contains a large number of upper limits, or *censored data*. Running correlation tests on the dataset is not a trivial matter, as standard statistical theory is not equipped to handle this kind of information.

Statisticians have extensively studied the problem of censored datasets, and a means for successfully handling them has been known for decades. It is called *survival analysis* and it allows censored data samples to be treated in a meaningful manner with minimal loss of information - the values of the upper/lower limits are formally taken into account when calculating correlation coefficients and other test statistics.

The application of survival analysis to astronomical data is outlined in two papers: Feigelson & Nelson 1985 (Paper I) and Isobe, Feigelson, & Nelson 1986 (Paper II). Paper I deals with univariate problems. Paper II considers bivariate techniques to characterise the correlation and line-regression between two variables. The test statistics described in these papers are available in the software package ASURV Rev. 1.1 (Isobe & Feigelson 1990; LaValley, Isobe & Feigelson 1992).

ASURV contains three different correlation tests - Cox's Proportional Hazard Model, Generalized Kendall's Tau, and Generalized Spearman's Rho. All three methods test the null hypothesis that *no correlation is present*. The ASURV routines compute the probability of the null hypothesis being true, P , also referred to as the significance of the correlation. The convention to be adopted here is that X and Y are correlated if $P \leq 5$ per cent. A correlation will be treated as firm if all three tests yield $P \leq 5$ per cent; the existence of a correlation will be treated as possible, but unconfirmed, if only some of the tests indicate $P \leq 5$ per cent.

Note, the Cox test only allows censoring in the dependent variable; the Kendall and Spearman tests allow censor-

ing in both the dependent and the independent variables. The Spearman technique has not been properly tested yet. It is known to give misleading results if $N < 30$.

7.1.2 Correlations for the entire dataset

Initially, the entire sample was used to run the correlation tests. The results of this analysis are given in Table 7.

Figure 4 predicts that the 850- μm flux density will mirror the 850- μm luminosity if $\Omega_o=1.0$. This is reflected by the $S_{850\mu m}$ - z and $L_{850\mu m}$ - z correlations having similar significances. As expected, decreasing Ω_o to 0.1 increases the strength of the $L_{850\mu m}$ - z correlation.

The absence of a correlation between P_{151MHz} and D_{linear} is indicative of a combined sample in which, as discussed by Willott et al. (1999), P_{151MHz} can be taken to crudely track jet power, and D_{linear} to crudely track source age.

It is troublesome, but not unexpected, that $L_{850\mu m}$, P_{151MHz} , and z are all correlated with each other. The strength of these correlations is greater in a low- Ω_o Universe. The strong correlation between P_{151MHz} and z could be responsible for either the $L_{850\mu m}$ - z correlation if $L_{850\mu m}$ actually correlates with P_{151MHz} , or for the $L_{850\mu m}$ - P_{151MHz} correlation if $L_{850\mu m}$ actually correlates with z . Thus, if the effects of cosmological evolution and radio power are to be disentangled, the entire dataset cannot be used.

$L_{850\mu m}$ also appears correlated with α_{radio} . However, this may be a remnant of the fact that α_{radio} and $L_{850\mu m}$ are both correlated with P_{151MHz} and z . Again, if the entire dataset is used, discriminating between different effects is difficult.

It was decided to choose a strip in the P - z plane that covered a large range of redshifts in a single narrow band of radio power. In the absence of a correlation between P_{151MHz}

Table 8. Results of the survival analysis correlation tests applied to Subset A. The significance (P) is the probability of the null hypothesis (*no correlation*) being true. The generalized Spearman test has not been applied as it breaks down if the sample size is less than 30. If both Cox and Kendall yield $P \leq 5$ per cent, the variables are taken to be correlated. If only one of them yields $P \leq 5$ per cent, evidence for a correlation is taken to be uncertain.

Cosmology	Variable		Percentage of Data Censored	Significance (P)			Correlation Present?
	Dependent	Independent		Cox	Kendall	Spearman	
$\Omega_0 = 1.0$	$S_{850\mu m}$	z	67%	0.29%	4.05%	—	YES
	D_{linear}	$\log(P_{151MHz})$	0%	63.20%	34.86%	—	NO
	$\log(P_{151MHz})$	z	0%	74.43%	50.65%	—	NO
	$\log(L_{850\mu m})$	$\log(P_{151MHz})$	67%	50.52%	77.71%	—	NO
	$\log(L_{850\mu m})$	z	67%	1.91%	15.70%	—	MAYBE
	$\log(L_{850\mu m})$	α_{radio}	67%	70.37%	85.01%	—	NO
	α_{radio}	$\log(P_{151MHz})$	0%	21.03%	16.40%	—	NO
	α_{radio}	z	0%	21.22%	18.32%	—	NO
Total Number of Galaxies: 21							

Table 9. Results of the survival analysis correlation tests applied to Subset B. The significance (P) is the probability of the null hypothesis (*no correlation*) being true. The generalized Spearman test has not been applied as it breaks down if the sample size is less than 30. If both Cox and Kendall yield $P \leq 5$ per cent, the variables are taken to be correlated. If only one of them yields $P \leq 5$ per cent, evidence for a correlation is taken to be uncertain.

Cosmology	Variable		Percentage of Data Censored	Significance (P)			Correlation Present?
	Dependent	Independent		Cox	Kendall	Spearman	
$\Omega_0 = 0.1$	$S_{850\mu m}$	z	65%	0.81%	5.87%	—	MAYBE
	D_{linear}	$\log(P_{151MHz})$	0%	84.35%	49.54%	—	NO
	$\log(P_{151MHz})$	z	0%	34.86%	27.00%	—	NO
	$\log(L_{850\mu m})$	$\log(P_{151MHz})$	65%	79.95%	96.22%	—	NO
	$\log(L_{850\mu m})$	z	65%	0.13%	2.01%	—	YES
	$\log(L_{850\mu m})$	α_{radio}	65%	64.95%	92.43%	—	NO
	α_{radio}	$\log(P_{151MHz})$	0%	0.39%	2.49%	—	YES
	α_{radio}	z	0%	20.64%	41.66%	—	NO
Total Number of Galaxies: 20							

and z , it could then be determined whether $L_{850\mu m}$ truly correlates with z or P_{151MHz} . The strip was chosen to satisfy the following criteria:

- (i) To cover the largest range in redshift possible whilst still maintaining even coverage of radio power. This automatically imposed the restriction that $z > 1.4$ due to the 3C survey having a lack of low-redshift, very high radio-power sources.
- (ii) To contain at least 20 objects to satisfy the requirements of the survival analysis techniques.

Initially a strip was chosen using the P - z plane for $\Omega_0=1.0$, hereafter referred to as Subset A. A different but similar strip was chosen from the P - z plane for $\Omega_0=0.1$. It will be referred to as Subset B. The sources included in each subset are listed in Table 6.

It is important to note that there is nothing special about the strips. They have merely been chosen to help disentangle the various influences affecting $L_{850\mu m}$. The results found for the subsets should apply to the entire sample and to radio galaxies in general.

7.1.3 Correlations for Subset A

Subset A, shown in Figure 2, contains 21 radio galaxies and is defined by $z > 1.4$ and $27.9 < \log(P_{151MHz}) < 28.5$ for $\Omega_0=1.0$, $H_0 = 50 \text{ km s}^{-1} \text{ Mpc}^{-1}$.

Table 8 contains the results of the survival analysis applied to Subset A, and Figure 5 contains the corresponding scatter plots.

For $\Omega_0=1.0$, the existence of a correlation between $L_{850\mu m}$ and redshift is hinted at, but is not confirmed by all of the correlation tests. The important point, however, is that $L_{850\mu m}$ definitely fails to correlate with P_{151MHz} and α_{radio} . The probability of ‘no correlation’ between $L_{850\mu m}$ and z is much lower than for $L_{850\mu m}$ - P_{151MHz} or $L_{850\mu m}$ - α_{radio} .

Survival analysis could also be applied to Subset A for the $\Omega_0=0.1$ case. However, for Subset A, P_{151MHz} and z are correlated if $\Omega_0=0.1$. This is precisely what was trying to be avoided by selecting the subset in the first place. Thus, a separate subsample will need to be chosen to study the statistics for a low- Ω_0 Universe.

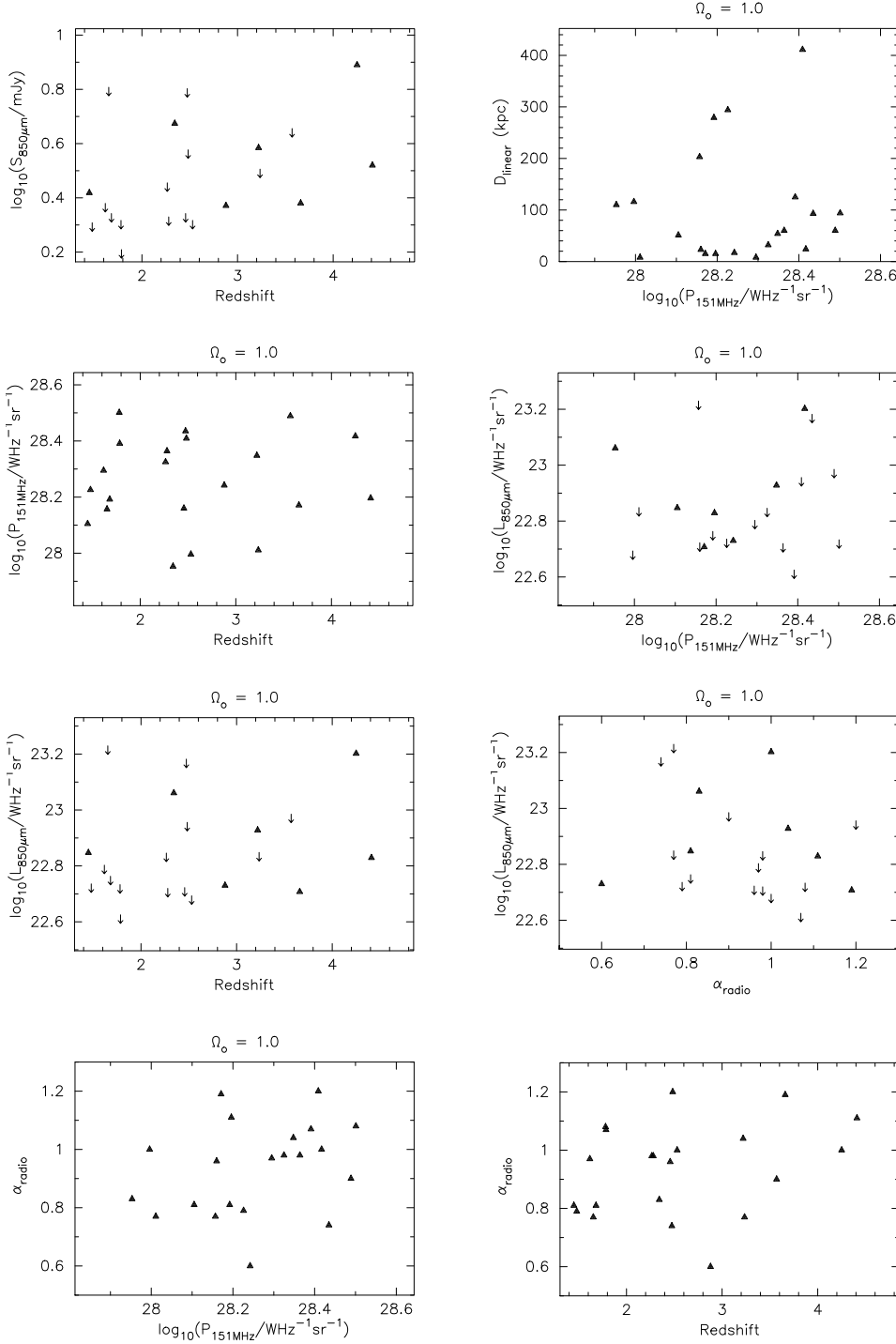


Figure 5. Scatter plots corresponding to the correlations investigated for Subset A.

7.1.4 Correlations for Subset B

Subset B, shown in Figure 2, contains 20 radio galaxies and is defined by $z > 1.4$ and $28.2 < \log(P_{151\text{MHz}}) < 28.9$ for $\Omega_0=0.1$, $H_0 = 50 \text{ km s}^{-1} \text{ Mpc}^{-1}$.

Table 9 contains the results of the survival analysis applied to Subset B, and Figure 6 contains the corresponding scatter plots.

The results of the survival analysis are more clear cut

in a low- Ω_0 Universe. The suspected correlation between $L_{850\mu\text{m}}$ and z is confirmed as significant by all of the correlation tests. Neither z nor $L_{850\mu\text{m}}$ correlates with $P_{151\text{MHz}}$. This indicates that the important correlation for $L_{850\mu\text{m}}$ is most likely to be with redshift, *not* radio luminosity.

For Subset B, $L_{850\mu\text{m}}$ does not correlate with α_{radio} or $P_{151\text{MHz}}$. However, α_{radio} and $P_{151\text{MHz}}$ correlate with each other. This implies that the correlation between α_{radio} and

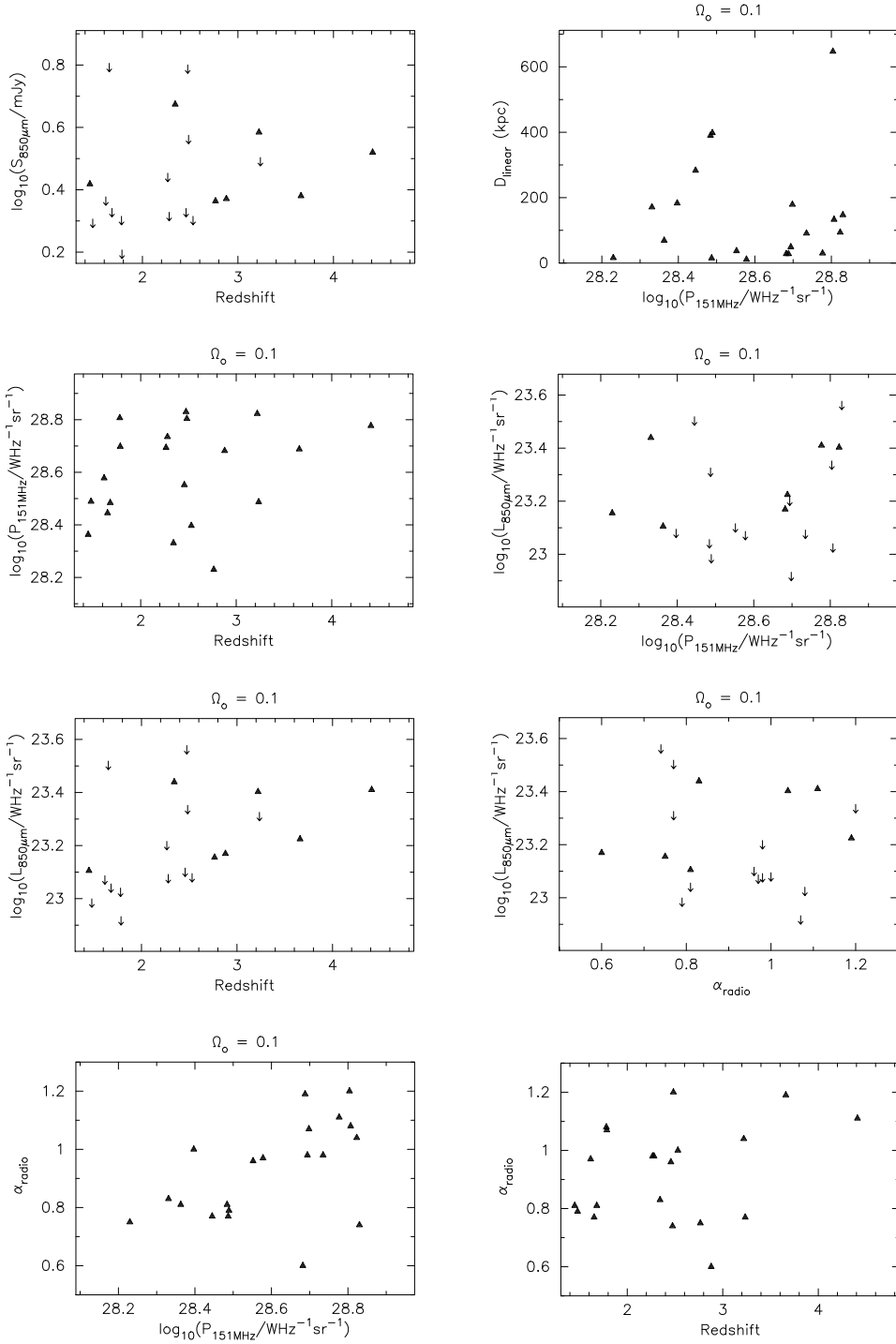


Figure 6. Scatter plots corresponding to the correlations investigated for Subset B.

$L_{850\mu m}$ seen for the entire dataset is an artifact of their mutual correlation with $P_{151\text{MHz}}$.

7.1.5 Considering the dust emission template

The analysis described so far assumes a template for dust emission with $\beta = 1.5$ and $T_{\text{dust}} = 40\text{K}$. However, what if this template was incorrect? Would the results of the analysis be affected if the true values of β and T_{dust} were different?

It has already been observed that increasing β and T_{dust} makes SCUBA more sensitive to submillimetre emission at $z = 4$ than it is at $z = 1$. Given the measured fluxes, the $850\text{-}\mu\text{m}$ luminosities at $z = 3 - 4$ will be reduced relative to those at $z = 1 - 2$ if β and T_{dust} are increased. As a result, correlations between $L_{850\mu m}$ and z should be weakened. Likewise, decreasing β and T_{dust} should strengthen $L_{850\mu m}\text{-}z$ correlations.

Changing β and T_{dust} will not alter $L_{850\mu m}$ in a radio-

Table 10. Summary of the $L_{850\mu m}$ - z correlation analysis for the two cosmologies considered and for reasonable values of β . ✓ indicates the survival analysis found a correlation between $L_{850\mu m}$ and z , ✗ indicates the survival analysis found no such correlation, and ? indicates that some, but not all, of the correlation tests found a correlation to be present.

$\Omega_o = 1.0$		$\Omega_o = 0.1$	
Dataset	Subset A	Dataset	Subset B
$\beta = 1.0$	✓	✓	✓
$\beta = 1.5$	✓	?	✓
$\beta = 2.0$	✓	✗	✓

power or radio-spectral index dependent manner. If the dust template is wrong, the correlations between $L_{850\mu m}$ and $P_{151\text{MHz}}/\alpha_{radio}$ should not be affected in a systematic way.

In order to investigate this fully, the survival analysis was re-run using several different combinations of β and T_{dust} . To examine the effect of changing β , T_{dust} was held at 40 K while β was increased to 2.0, and decreased to 1.0. Likewise, β was held at 1.5 while T_{dust} was changed to 100 K, 70 K, and 20 K.

The observed effects on the results of the correlation tests can be summarised as follows:

(i) $L_{850\mu m}$ - z : Increasing β or T_{dust} destroys the marginal correlation between $L_{850\mu m}$ and z for Subset A. For the entire dataset (both cosmologies) and for Subset B, the correlation is evident regardless of the values of β and T_{dust} . Decreasing β and T_{dust} confirms the possible $L_{850\mu m}$ - z correlation for Subset A.

(ii) $L_{850\mu m}$ - $P_{151\text{MHz}}$: Changing β and T_{dust} does not destroy the $L_{850\mu m}$ - $P_{151\text{MHz}}$ correlation for the entire dataset, nor does it create a correlation between $L_{850\mu m}$ and $P_{151\text{MHz}}$ for Subsets A or B.

(iii) $L_{850\mu m}$ - α_{radio} : Changing β and T_{dust} does not destroy the $L_{850\mu m}$ - α_{radio} correlation for the entire dataset, nor does it create a correlation between $L_{850\mu m}$ and α_{radio} for Subsets A or B.

7.1.6 Summary of correlation analysis

For Subsets A and B, survival analysis finds $L_{850\mu m}$ to be correlated with redshift unless the highest values of β and Ω_o are chosen (Table 10). Furthermore, $L_{850\mu m}$ is not found to correlate with either $P_{151\text{MHz}}$ or α_{radio} for any of the tested cosmologies or dust emission templates. Even for high values of β and Ω_o , there is evidence that $L_{850\mu m}$ is dependent on redshift instead of on the radio properties of the source: the probability of ‘no correlation’ is substantially smaller for $L_{850\mu m}$ and z than for $L_{850\mu m}$ and $P_{151\text{MHz}}$ or α_{radio} .

This all suggests that the correlation between $L_{850\mu m}$ and redshift for the entire dataset is real, and is not an artifact of their mutual correlation to $P_{151\text{MHz}}$ (although this may affect the strength of the observed $L_{850\mu m}$ - z correlation).

Given the low detection threshold adopted in this paper, it is worth re-iterating that a detection threshold of $S/N > 3$ (with upper limits taken at the 3σ level) yields the same result.

Table 11. Detection rate of radio galaxies at $850\mu m$ for $z < 2.5$ and $z > 2.5$. For each dataset and redshift interval, the number of galaxies present is given in parenthesis. Note, 6C1159+36 may be at a lower redshift than previously published, which would increase the detection rate at $z > 2.5$.

Dataset	Detection Rate	
	$z < 2.5$	$z > 2.5$
Subset A	15% (13)	63% (8)
Subset B	15% (13)	71% (7)
All Data	12% (33)	77% (13)

7.2 Further investigations of the relationship between $L_{850\mu m}$ and redshift

SCUBA has had more success detecting the higher-redshift galaxies in the sample. This is shown in Table 11, which display the $850\mu m$ detection rate for $z < 2.5$ and $z > 2.5$. At $850\mu m$, SCUBA is almost equally sensitive to all of the galaxies in the sample. The striking result that almost none of the galaxies are detected if $z < 2.5$, whereas almost all of them are detected if $z > 2.5$, suggests a trend of increasing submillimetre luminosity with redshift. Note, the detection rates observed for Subset A and Subset B closely mirror those found for the entire sample, providing further evidence for the cosmological evolution of the radio galaxy population irrespective of the radio source.

There is an alternative to survival analysis for investigating the relationship between $L_{850\mu m}$ and z . Instead of running a correlation test which only takes the strength of the detection or upper-limit into account, the $850\mu m$ luminosities can be binned in redshift to calculate the typical submillimetre luminosity as a function of redshift. This method considers both the signal and error for each source and is independent of the precise choice of detection threshold. Note, for the following discussion, H_o has been taken to be $67\text{ km s}^{-1}\text{Mpc}^{-1}$ for $\Omega_o = 0.1$; this should give a comparable measure of luminosity to the $\Omega_o = 1.0$, $H_o = 50\text{ km s}^{-1}\text{Mpc}^{-1}$ cosmology.

Four redshift bins have been chosen which are adequately sampled by the dataset and are centered as near as possible on $z = 1, 2, 3, 4$: $0.45 \leq z < 1.45$, $1.45 \leq z < 2.45$, $2.45 \leq z < 3.45$, and $3.45 \leq z < 4.45$. The weighted-mean (Bevington 1969) $850\mu m$ luminosity, $\langle L_{850\mu m} \rangle$, is plotted in Figure 7 for the entire dataset and Subset A assuming an $\Omega_o = 1.0$ cosmology and for the entire dataset and Subset B assuming an $\Omega_o = 0.1$ cosmology. Curves of the form $L = a(1+z)^b$ have been fit to $\langle L_{850\mu m} \rangle$ in order to help quantify the strength of the $850\mu m$ luminosity evolution.

There are several important points to be made from Figure 7:

(i) For the entire dataset, there are clear steps in $\langle L_{850\mu m} \rangle$ between each redshift bin. If this trend is characterised by the function $L = a(1+z)^b$, nonlinear least-squares fitting indicates that $b = 4.58 \pm 0.52$ if $\Omega_o = 1.0$, and $b = 5.52 \pm 0.53$ for $\Omega_o = 0.1$.

(ii) For Subset A, there are clear steps in $\langle L_{850\mu m} \rangle$ between the $z = 2$ and $z = 3$ bins, and between the $z = 3$ and $z = 4$ bins. If this trend is characterised by the function $L = a(1+z)^b$, nonlinear least-squares fitting indicates that

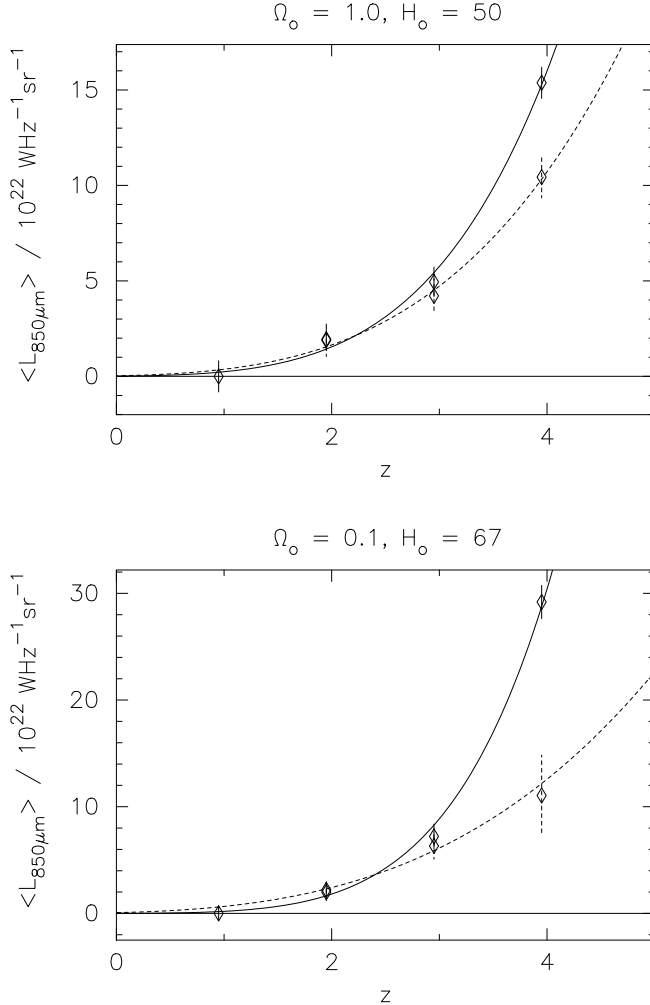


Figure 7. Weighted-mean 850- μ m luminosity, $\langle L_{850\mu m} \rangle$, binned in redshift. $\langle L_{850\mu m} \rangle$ has been plotted at the midpoint of each bin, which at most varies by 0.2 from the average redshift of all the objects in the bin. The error bars only represent the statistical errors on the observations; they do not account for uncertainties in either the cosmology or the dust template. Curves of the form $L = a(1+z)^b$ have been fit to the data using nonlinear least-squares fitting, and the horizontal line indicates the origin (or $L_{850\mu m} = 0.0$). The upper plot displays an $\Omega_0 = 1.0$, $H_0 = 50$ km s $^{-1}$ Mpc $^{-1}$ cosmology, and $\langle L_{850\mu m} \rangle$ is plotted for both the entire dataset and Subset A (diamond symbols). The solid curve is the best-fit for the entire dataset, with $a = 0.010 \pm 0.008$, $b = 4.58 \pm 0.52$, $\chi^2 = 1.23$. The dashed curve is the best-fit for Subset A, with $a = 0.029 \pm 0.034$, $b = 3.67 \pm 0.76$, $\chi^2 = 0.29$. Similarly, the lower plot displays the entire dataset and Subset B (diamond symbols) for an $\Omega_0 = 0.1$, $H_0 = 67$ km s $^{-1}$ Mpc $^{-1}$ cosmology. The solid curve is the best-fit for the entire dataset, with $a = 0.004 \pm 0.003$, $b = 5.52 \pm 0.53$, $\chi^2 = 1.58$. The dashed curve is the best-fit for Subset B, with $a = 0.070 \pm 0.099$, $b = 3.23 \pm 1.01$, $\chi^2 = 0.32$. Subsets A and B do not contain any objects in the $z = 1$ bin.

$b = 3.67 \pm 0.76$. Subset A does not contain any objects in the $z = 1$ bin.

(iii) For Subset B, there is a clear step in $\langle L_{850\mu m} \rangle$ between the $z = 2$ and $z = 3$ bins. There may also be an increase in $\langle L_{850\mu m} \rangle$ from $z = 3$ to $z = 4$, although the error bars do not preclude $\langle L_{850\mu m} \rangle$ flattening off between these two redshifts. If the model $L = a(1+z)^b$ is assumed, nonlinear least-squares fitting indicates that $b = 3.23 \pm 1.01$. Subset B does not contain any objects in the $z = 1$ bin.

(iv) For Subsets A and B, the correlation analysis has revealed that $L_{850\mu m}$ does not depend on the radio properties of the source. These subsamples are not special, they have been chosen to cover an even spread in radio luminosity over a range of redshifts; their selection has been dictated only by the deficiencies of the original radio surveys. Thus, the evolu-

tion of $\langle L_{850\mu m} \rangle$ with redshift observed for these two subsamples, which is consistent with $\langle L \rangle \sim (1+z)^3$, should apply to all radio galaxies. This is supported by the fact that for the $z = 2$ and $z = 3$ bins, the value of $\langle L_{850\mu m} \rangle$ for the subset mimics the value of $\langle L_{850\mu m} \rangle$ for the entire dataset. At $z \sim 4$, however, some of the most extreme objects in the Universe have been observed (e.g. 4C60.07 and 4C41.17), which are simultaneously the most radio-luminous and the most submillimetre-luminous, residing at the highest redshifts. These galaxies fall outside the subsets which have been constructed to exclude radio-luminosity bias. Thus at $z \sim 4$, $\langle L_{850\mu m} \rangle$ for the entire sample far exceeds that of the subsets.

As for the correlation analysis, it is important to investigate the robustness of this result to variations in the

dust template. Thus, β was changed to 1.0 and 2.0, whilst T_{dust} was fixed at 40K. Likewise, holding β constant at 1.5, T_{dust} was changed to 20K, 70K, and 100K. Altering the dust template has a larger effect on the higher redshift sources. Thus, if β and T_{dust} are increased, the trend of increasing $\langle L_{850\mu\text{m}} \rangle$ with redshift is weakened; if they are decreased the trend is strengthened. More specifically, it was found that:

- (i) For the entire dataset, there are always clear steps in $\langle L_{850\mu\text{m}} \rangle$ between all redshift bins, regardless of the values of β and T_{dust} .
- (ii) For Subset A, there is always a clear step in $\langle L_{850\mu\text{m}} \rangle$ between $z = 2$ and $z = 3$ and between $z = 3$ and $z = 4$, regardless of the values of β and T_{dust} .
- (iii) For Subset B, there is always a clear step in $\langle L_{850\mu\text{m}} \rangle$ between $z = 2$ and $z = 3$. The possible step between $z = 3$ and $z = 4$ becomes clear (i.e. the error bars do not allow $\langle L_{850\mu\text{m}} \rangle$ to remain flat) if β is decreased to 1.0 or if T_{dust} is decreased to 20K.
- (iv) For the $z = 2$ and $z = 3$ bins, $\langle L_{850\mu\text{m}} \rangle$ for the entire dataset always closely mimics $\langle L_{850\mu\text{m}} \rangle$ for the subsets, regardless of the values of β and T_{dust} .
- (v) Adopting the model $L = a(1+z)^b$, the luminosity evolution observed for Subsets A and B upon changing β and T_{dust} is consistent with ‘b’ lying between 2.5 and 5.0.

Binning the data has been able to confirm the relationship between $L_{850\mu\text{m}}$ and z that was initially suggested by survival analysis. It is therefore possible that binning may also reveal a relationship between $L_{850\mu\text{m}}$ and $P_{151\text{MHz}}$ or α_{radio} .

It is only necessary to check this for Subsets A and B, as $L_{850\mu\text{m}}$ is known to be strongly correlated with both $P_{151\text{MHz}}$ and α_{radio} for the entire dataset. If $L_{850\mu\text{m}}$ remains independent of the radio source for Subsets A and B, the evidence for evolution with redshift will be strengthened.

Binning $L_{850\mu\text{m}}$ against radio power and radio spectral index fails to reveal a dependence of $L_{850\mu\text{m}}$ on the radio source. Altering the dust template does not change this result.

7.3 Addressing potential remaining selection effects

7.3.1 Potential contamination by obscured quasars

Careful scrutiny of the $P-z$ plane defined by combining all the known high-redshift radio sources shows that there is a lack of high-redshift, high-radio power quasars, although this is at least partly due to the selection effects inherent in steep-spectrum-selected radio samples (Jarvis et al., in preparation). This is also the area of the $P-z$ plane where the $850\mu\text{m}$ detections of the radio-galaxy sample are clustered.

According to Unified Schemes, radio-loud quasars and radio galaxies are identical phenomena: the former is viewed within the opening angle of an obscuring dust torus allowing the quasar to be seen, the latter is viewed outside the opening angle of the dust torus which hides the quasar from view (e.g. Antonucci & Barvainis 1990 and references therein).

It can be argued that at higher redshifts, there is an increased chance of dust hiding the optically-bright nucleus of a radio-loud quasar, even though the radio-loud quasar is

viewed within the opening angle of the dust torus. Thus, potentially, several high-redshift radio-loud quasars may have been mis-classified as radio galaxies. Therefore, the worry for the present study is that our radio galaxy sample could become progressively more contaminated by obscured quasars with increasing redshift.

Of course, within unified schemes all powerful radio galaxies contain a buried quasar. Thus the point of issue for the present study is whether the submillimetre emission of a powerful radio source is orientation dependent. If so, and if our sample was progressively contaminated by mis-classified radio-loud quasars with redshift, it could account for the observed increase of $L_{850\mu\text{m}}$ with redshift. Given the above considerations, this might happen because, for example, some of our high-redshift objects might be observed in a line of sight sufficiently close to the jet axis that the contribution from a more face-on quasar heated torus (which may be optically thick in the rest-frame mid-far infrared) becomes dominant at $850\mu\text{m}$.

One way to resolve this issue is to check directly whether unification works at submillimetre wavelengths, and we are currently undertaking a programme of SCUBA observations of radio-loud quasars to test this hypothesis. However, even if radio-loud quasars and radio galaxies are shown to differ at submillimetre wavelengths this need not invalidate the conclusions of this study, provided we can demonstrate that progressive quasar contamination with increasing redshift is not a problem.

We can in fact test the likelihood of this selection effect directly using the basic radio properties of the objects we have observed with SCUBA. In Figure 8, the rest-frame 15 GHz core:lobe ratio is plotted against redshift and $L_{850\mu\text{m}}$ for our sample. If the high-redshift objects in the sample are in fact buried radio-loud quasars masquerading as galaxies, they should be expected to display systematically higher radio core:lobe ratios, owing to Doppler boosting of the radio core along the line of sight. The typical core:lobe ratio does not appear to change significantly with redshift, and so this analysis does not support the idea of a systematic bias towards buried quasars at high redshift within the SCUBA radio galaxy sample studied here. Moreover, there is no evidence that the more core dominated objects are more detectable with SCUBA.

These mis-classified buried quasars may exist. Two of the objects in our sample, 6C0902+34 and 4C23.56, appear significantly more core-dominated than the rest, and are likely candidates since their core:lobe radio is comparable ($\simeq 10$ per cent) to that typically displayed by radio quasars (Spencer et al. 1991). Furthermore, 6C0902+34 has a single-sided radio jet characteristic of a radio-loud quasar (Carilli 1995a). In addition to the evidence at radio wavelengths, 4C23.56 has a polarized ultraviolet continuum consistent with scattered quasar light (Cimatti et al. 1998a). It is worth noting that the core:lobe ratio in these two sources is an order of magnitude higher than the typical value throughout the rest of the radio galaxy sample. Moreover, in any case, SCUBA failed to detect dust emission from either one.

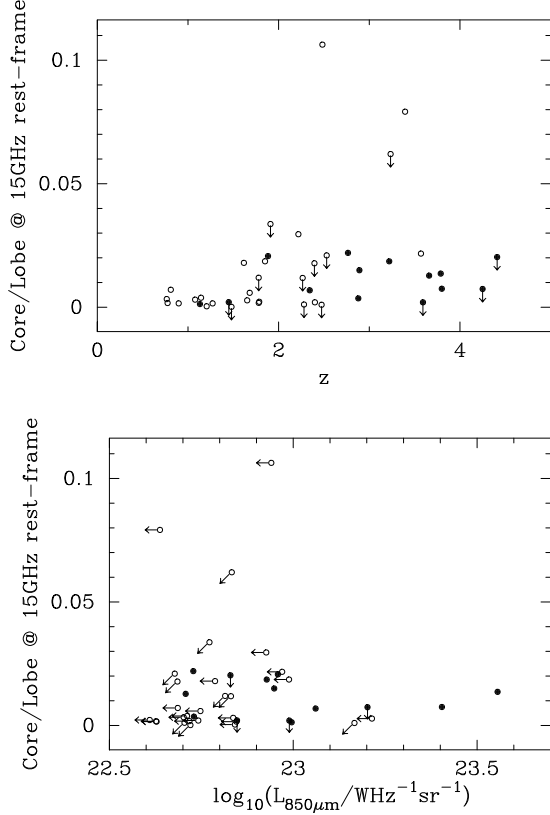


Figure 8. Investigation of the rest-frame 15 GHz core:lobe ratio for the objects in our sample. The top plot shows the core:lobe ratio against redshift. Solid circles represent the sources detected with SCUBA, and open circles represent the non-detections. Down arrows indicate sources for which no radio core has been detected. In order to estimate the core flux at 15 GHz rest-frame, the core spectral index is required. For sources with more than one core detection, we have measured this spectral index. For sources with only one core detection, we have assumed the core to be flat. The bottom plot compares the core:lobe ratio with the 850- μ m luminosity. An $\Omega_0=1.0$ cosmology is assumed; there is no significant difference between this plot and one for which $\Omega_0=0.1$.

7.3.2 Preferential selection of young radio sources at high redshift

All realistic models of the time evolution of classical double radio sources (e.g. Kaiser et al. 1997; Blundell et al. 1999; Blundell & Rawlings 1999) predict that their lobe luminosities decline with age once they are large enough to avoid synchrotron self-absorption. Older sources are thus (obviously) more likely to fall below the flux limit of a given survey if they reside at high redshift. A single flux-limited survey may thus be biased towards young radio sources at high redshift, whereas at lower redshifts a large range of radio source ages will be included in the same survey.

The importance of this selection effect to our SCUBA survey is probably not a major concern for two reasons. First, the target sources are *not* selected from a single flux-limited sample, but rather are selected rather close to the flux-density limit of progressively deeper surveys - in other words at $z \simeq 4$ the radio sources must be preferentially young, but the sources we have studied at, say, $z \simeq 1.5$ must also be fairly young to enter the brighter 3CRR sample

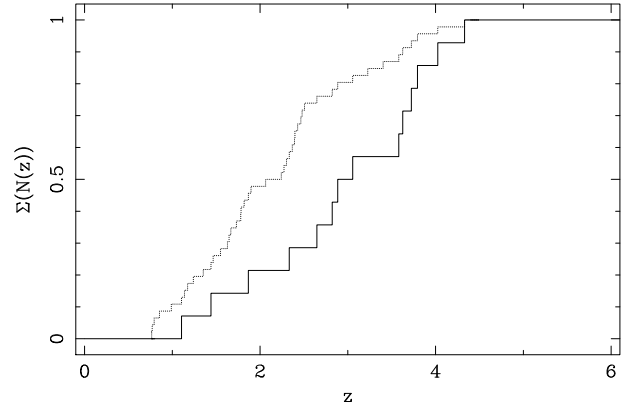


Figure 9. The cumulative redshift distribution of the radio galaxy sample. The dotted line is for the entire sample, the solid line only considers the galaxies detected at 850 μ m. For the detections, the median redshift of the distribution is $< z > = 3.1$.

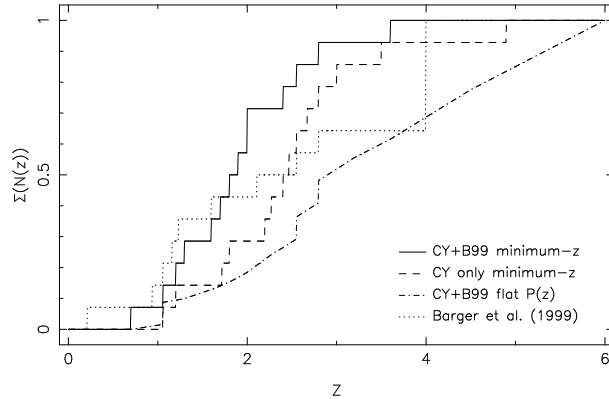


Figure 10. Figure 2 of Smail et al. 2000b. The full caption, as it appears in the original paper, is as follows: “Cumulative redshift distribution for the full submm sample. We have used the spectroscopic redshifts of those sources thought to be reliable (Table 1) and combined these with the probable redshift ranges of the remaining sources derived from their $\alpha_{1.4}^{850}$ indices or limits. The solid line shows the cumulative distribution if we assume the minimum redshift distribution that is obtained if all sources lie at their lower z_α limit given in Table 1 (dashed line is the equivalent analysis but restricted to the CY models). The effect of non-thermal radio emission, which drives down the $\alpha_{1.4}^{850}$ indices, means that this is a very conservative assumption if some fraction of the population harbor radio-loud AGNs. The dash-dotted line assumes a flat probability distribution for the sources within their z_α ranges and a maximum redshift of $z = 6$ for those sources where we only have a lower limit on $\alpha_{1.4}^{850}$. Finally, the dotted line is the cumulative redshift distribution from Barger et al. (1999a) with two of the source identifications corrected as in Smail et al. (1999) and all blank-field/extremely red object candidates placed at $z = 4$.”

from which our lower-redshift targets are selected. This fact will undoubtedly weaken any correlation of source age with redshift (certainly at $z > 1$), compared with that expected from a single flux-limited survey as described by Blundell & Rawlings (1999).

Second, even if some residual correlation between radio-source youthfulness and redshift remains in our sample, it

is not clear that this has any implications whatsoever for this submillimetre study. For it to be responsible for the trend of increasing $L_{850\mu\text{m}}$ with z , radio-source age must be intimately linked to starburst luminosity. Our data do not provide any evidence in support of this. For example, one of the largest radio sources, and hence possibly one of the oldest, 6C0905+39, was detected by SCUBA. To examine this more thoroughly, survival analysis was applied to test for correlations between D_{linear} (taken as indicative of the age of the radio source), z , and $L_{850\mu\text{m}}$. As found for complete samples by Blundell et al. (1999), we find a negative correlation between D_{linear} and z . However, no evidence for a correlation between D_{linear} and $L_{850\mu\text{m}}$ was found (correlation tests yield a significance of ~ 40 per cent). We therefore find no internal evidence in support of the hypothesis that $L_{850\mu\text{m}}$ is closely linked to radio-source age, although the mildness of the $D_{\text{linear}}:z$ correlation means that caution is advised in attempting to interpret D_{linear} as a reliable estimator of radio-source age (Blundell et al. 1999; Blundell & Rawlings 1999).

8 CONCLUDING REMARKS

In summary, our attempts to investigate and quantify the various possible biases which might conceivably afflict this study have simply served to reaffirm and strengthen our basic result, namely that the submillimetre luminosity of radio galaxies is primarily a function of redshift as illustrated in Figure 7.

It therefore seems hard to avoid the straightforward conclusion that the observed increase in submillimetre detection rate and characteristic luminosity with redshift is due to the increasing youthfulness of the stellar populations of the radio galaxies in our sample.

In a separate paper we will explore how the inferred evolution of gas mass and star-formation rate in these galaxies compares with the predictions of models of elliptical galaxy formation and evolution. However, it is interesting to briefly consider whether the apparently rather extreme evolution is peculiar to radio galaxies, or may in fact be typical of the cosmological evolution of dust and gas in massive ellipticals in general.

In Figure 9 we show the cumulative redshift distribution of our radio galaxy sample, along with the cumulative redshift distribution of the subset detected at submillimetre wavelengths. This figure serves to re-emphasize that the high median redshift of our detected galaxies ($z = 3$) does not simply reflect the median redshift of the sample selected for observation ($z = 2$). However, what is particularly interesting is that the redshift distribution of our submillimetre detected radio galaxies is statistically indistinguishable from current best estimates of the redshift distribution of sources detected in SCUBA surveys, as illustrated in Figure 10 (Smail et al. 2000b). This comparison provides at least circumstantial evidence that the submillimetre evolution of radio galaxies found here may indeed be symptomatic of the evolution of massive elliptical galaxies in general.

At first sight, it may appear contradictory that the average submillimetre luminosity of the radio galaxy sample continues to rise beyond $z \sim 3$ while the median redshift of the sample is $z \sim 3$. This results from the median redshift

of our most luminous detections being higher at $z \sim 3.6$ for sources brighter than 5 mJy.

This raises the interesting possibility that the most massive dust-enshrouded starbursts are confined to $z > 3$. Therefore the median redshift of submillimetre sources detected in blank-field surveys may prove to be a function of flux density.

It will be some time before the redshift information in bright submillimetre surveys approaches that currently available for radio-selected samples. However, it will undoubtedly be very interesting to see how this comparison evolves as submillimetre-selected samples are studied and refined in the years to come.

ACKNOWLEDGMENTS

We wish to thank the staff of the James Clerk Maxwell Telescope, particularly Wayne Holland, Tim Jenness, Graeme Watt and all the T.S.S.s, for all their help. Many thanks to Katherine Blundell for allowing us access to radio data prior to publication. Figure 2 of Smail et al. 2000b, and the corresponding caption text, have been reproduced by permission of the AAS. This research has made use of the NASA/IPAC Extragalactic Database, which is operated by the Jet Propulsion Laboratory, Caltech, under contract with the National Aeronautics and Space Administration. ENA, DHH and RJI acknowledge support from the UK Particle Physics and Astronomy Research Council (PPARC). The JCMT is operated by the Joint Astronomy Centre, on behalf of PPARC, the Netherlands Organisation for Pure Research, and the National Research Council of Canada.

REFERENCES

Akujor C. E., Spencer R. E., Zhang F. J., Davis R. J., Browne I. W. A., Fanti C., 1991, MNRAS, 250, 215, (ASZ91)
 Andreani P., La Franca F., Cristiani S., 1993, MNRAS, 261, L35
 Antonucci R., Barvainis R., 1990, ApJ, 363, L17
 Archibald E. N., 1999, The cosmological evolution of dust and gas in radio galaxies, Ph.D. thesis, University of Edinburgh
 Barger A. J., Cowie L. L., Sanders D. B., 1999, ApJ, 518, L5
 Becker R. H., White R. L., Edwards A. L., 1991, ApJS, 75, 1, (BWE91)
 Benford D. J., Cox P., Omont A., Phillips T. G., McMahon R. G., 1999, ApJ, 518, L65, (BCO99)
 Bennett A. S., 1962, MmRAS, 68, 163
 Best P. N., Longair M. S., Röttgering H. J. A., 1997, MNRAS, 292, 758, (BLR97)
 Best P. N., Carilli C. L., Garrington S. T., Longair M. S., Röttgering H. J. A., 1998a, MNRAS, 299, 357, (BCG98)
 Best P. N. et al., 1998b, MNRAS, 301, L15, (BRB98)
 Bevington P. R., 1969, Data Reduction and Error Analysis for the Physical Sciences. McGraw-Hill
 Blain A. W., Ivison R. J., Smail I., Kneib J.-P., 1998, in Colombi S., Mellier Y., eds, Wide Field Surveys in Cosmology, 14th IAP meeting held May 26-30, 1998, Paris. Publisher: Editions Frontières. p. 364
 Blundell K. M., Rawlings S., 1999, Nature, 399, 330
 Blundell K. M., Rawlings S., Eales S. A., Taylor G. B., Bradley A. D., 1998, MNRAS, 295, 265, (BRE98)
 Blundell K. M., Rawlings S., Willott C. J., 1999, AJ, 117, 677
 Blundell K. M., Rawlings S., Riley J. M., Willott C. J., Laing R. A., 2000, New Astronomy, to be submitted, (BRR00)

Blundell K. M. et al., in preparation, (KB17)

Bunker A. J., 1996, Searches for distant galaxies, Ph.D. thesis, University of Oxford, (Bthesis)

Carilli C. L., 1995a, *A&A*, 298, 77

Carilli C. L., 1995b, *A&A*, 298, 77, (C95)

Carilli C. L., Owen F. N., Harris D. E., 1994, *AJ*, 107, 480, (COH94)

Carilli C. L., Röttgering H. J. A., van Ojik R., Miley G. K., van Breugel W. J. M., 1997, *ApJS*, 109, 1, (CRvO97)

Caswell J. L., Crowther J. H., 1969, *MNRAS*, 145, 181, (C&C69)

Chambers K. C., Miley G. K., van Breugel W. J. M., 1988, *ApJ*, 327, L47, (CMvB88)

Chambers K. C., Miley G. K., van Breugel W. J. M., 1990, *ApJ*, 363, 21, (CMvB90)

Chambers K. C., Miley G. K., van Breugel W. J. M., Bremer M. A. R., Huang J.-S., Trentham N. A., 1996, *ApJS*, 106, 247, (CMvB96)

Chini R., Krügel E., 1994, *A&A*, 288, L33, (C&K94)

Chini R., Krügel E., Kreytsa E., 1986, *A&A*, 167, 315

Cimatti A., di Serego Alighieri S., Vernet J., Cohen M. H., Fosbury R. A. E., 1998a, *ApJ*, 499, L21

Cimatti A., Freudling W., Röttgering H. J. A., Ivison R. J., Mazzei P., 1998b, *A&A*, 329, 399, (CFR98)

Condon J. J., Cotton W. D., Greisen E. W., Yin Q. F., Perley R. A., Taylor G. B., Broderick J. J., 1998, *AJ*, 115, 1693, (CC98)

Dey A., Spinrad H., Dickinson M., 1995, *ApJ*, 440, 515, (DSD95)

Djorgovski S., Spinrad H., Pedelty J., Rudnick L., Stockton A., 1987, *AJ*, 93, 1307, (DSP87)

Douglas J. N., Bash F. N., Bozian F. A., Torrence G. W., Wolfe C., 1996, *AJ*, 111, 1945, (DBB96)

Downes D., Solomon P. M., Sanders D. B., Evans A. S., 1996, *A&A*, 313, 91, (DSS96)

Draine B. T., Lee H. M., 1984, *ApJ*, 285, 89

Dunlop J. S., 1999, in Bunker A. J., van Breugel W. J. M., eds, ASP Conf. Ser. 193: The Hy-Redshift Universe: Galaxy Formation and Evolution at High Redshift. p. 133

Dunlop J. S., et al. 2000, *MNRAS*, in preparation

Dunlop J. S., Hughes D. H., Rawlings S., Eales S. A., Ward M. J., 1994, *Nature*, 370, 347, (DHR94)

Dunne L., Eales S., Edmunds M., Ivison R., Alexander P., Clements D. L., 2000, *MNRAS*, 315, 115

Eales S. A., 1985, *MNRAS*, 217, 149

Eales S. A., Edmunds M. G., 1996, *MNRAS*, 280, 1167

Eales S. A., Rawlings S., 1993, *ApJ*, 411, 67, (ER93)

Eales S. A., Rawlings S., 1996, *ApJ*, 460, 68, (ER96)

Eales S. A., Alexander P., Duncan W. D., 1989, *MNRAS*, 240, 817

Eales S. A., Rawlings S., Dickinson M., Spinrad H., Hill G. J., Lacy M., 1993, *ApJ*, 409, 578, (ERD93)

Eales S., Rawlings S., Law-Green D., Gotter G., Lacy M., 1997, *MNRAS*, 291, 593, (ERLG97)

Feigelson E. D., Nelson P. I., 1985, *ApJ*, 293, 192

Fernini I., Burns J. O., Bridle A. H., Perley R. A., 1993, *AJ*, 105, 1690, (F93)

Fernini I., Burns J. O., Perley R. A., 1997, *AJ*, 114, 2292, (FBP97)

Ficarra A., Grueff G., Tomassetti G., 1985, *A&AS*, 59, 255, (FGT85)

Frayer D. T., Brown R. L., 1997, *ApJS*, 113, 221

Gower J. F. R., Scott P. F., Wills D., 1967, *MmRAS*, 71, 49, (GSW67)

Gregory P. C., Condon J. J., 1991, *ApJS*, 75, 1011, (GC91)

Gregory P. C., Scott W. K., Douglas K., Condon J. J., 1996, *ApJS*, 103, 427, (GSDC96)

Griffith M. R., Wright A. E., Burke B. F., Ekers R. D., 1995, *ApJS*, 97, 347, (GWBE95)

Hales S. E. G., Baldwin J. E., Warner P. J., 1988, *MNRAS*, 234, 919, (6C-II)

Hales S. E. G., Masson C. R., Warner P. J., Baldwin J. E., 1990, *MNRAS*, 246, 256, (6C-III)

Hales S. E. G., Baldwin J. E., Warner P. J., 1993a, *MNRAS*, 263, 25, (6C-VI)

Hales S. E. G., Masson C. R., Warner P. J., Baldwin J. E., Green D. A., 1993b, *MNRAS*, 262, 1057, (6C-V)

Hales S. E. G., Waldrum E. M., Rees N., Warner P. J., 1995, *MNRAS*, 274, 447, (HWR95)

Helou G., Beichman C. A., 1990, in Kaldeich B., ed., From Ground-Based to Space-Borne Sub-mm Astronomy, ESA SP-314. p. 117

Hildebrand R. H., 1983, *QJRAS*, 24, 267

Holland W. S. et al., 1999, *MNRAS*, 303, 659

Hughes D. H., Gear W. K., Robson E. I., 1994, *MNRAS*, 270, 641

Hughes D. H., Dunlop J. S., Rawlings S., 1997, *MNRAS*, 289, 766, (HDR97)

Hughes D. H. et al., 1998, *Nature*, 394, 241

Isobe T., Feigelson E. D., 1990, *BAAS*, 22, 917

Isobe T., Feigelson E. D., Nelson P. I., 1986, *ApJ*, 306, 490

Ivison R. J., 1995, *MNRAS*, 275, L33, (I95)

Ivison R. J. et al., 1998a, *ApJ*, 494, 211, (IDHA98)

Ivison R. J., Smail I., Le Borgne J.-F., Blain A. W., Kneib J.-P., Bézecourt J., Kerr T. H., Davies J. K., 1998b, *MNRAS*, 298, 583

Ivison R. J., Dunlop J. S., Smail I., Dey A., Liu M. C., Graham J. R., 2000a, *ApJ*, accepted, astro-ph/0005234

Ivison R. J., Smail I., Barger A. J., Kneib J.-P., Blain A. W., Owen F. N., Kerr T. H., Cowie L. L., 2000b, *MNRAS*, 315, 209

Ivison R. J. et al., in preparation

Jarvis M. J. et al., in preparation, (Jprep)

Jenness T., Lightfoot J. F., Holland W. S., 1998, Proc. SPIE, 3357, 548

Kaiser C. R., Dennett-Thorpe J., Alexander P., 1997, *MNRAS*, 292, 723

Knapp G. R., Patten B. M., 1991, *AJ*, 101, 1609

Lacy M. D., 1992, Samples of radio sources selected at 38 MHz, Ph.D. thesis, University of Oxford, (Lthesis)

Lacy M., Rawlings S., 1994, *MNRAS*, 270, 431, (LR94)

Lacy M. et al., 1994, *MNRAS*, 271, 504, (LMR94)

Laing R. A., private communication, (Lpc)

Laing R. A., Peacock J. A., 1980, *MNRAS*, 190, 903, (LP)

Laing R. A., Riley J. M., Longair M. S., 1983, *MNRAS*, 204, 151, (LRL)

Large M. I., Mills B. Y., Little A. G., Crawford D. F., Sutton J. M., 1981, *MNRAS*, 194, 693, (LML81)

LaValley M., Isobe T., Feigelson E., 1992, in Worrall D. M., Biemesderfer C., Barnes J., eds, ASP Conf. Ser. 25: Astronomical Data Analysis Software and Systems I. Vol. 1, p. 245

Law-Green J. D. B., Eales S. A., Leahy J. P., Rawlings S., Lacy M., 1995a, *MNRAS*, 277, 995, (LGE95)

Law-Green J. D. B., Leahy J. P., Alexander P., Allington-Smith J. R., van Breugel W. J. M., Eales S. A., Rawlings S. G., Spinrad H., 1995b, *MNRAS*, 274, 939, (LLA95)

Lawrence C. R., Bennett C. L., Hewitt J. N., Langston G. I., Klotz S. E., Burke B. F., Turner K. C., 1986, *ApJS*, 61, 105, (LBH86)

Lilly S. J., 1988, *ApJ*, 333, 161, (L88)

Lilly S. J., 1989, *ApJ*, 340, 77

Lilly S. J., Longair M. S., 1984, *MNRAS*, 211, 833

Liu R., Pooley G., Riley J. M., 1992, *MNRAS*, 257, 545, (LPR92)

Magorrian J. et al., 1998, *AJ*, 115, 2285

Mathis J. S., Whiffen G., 1989, *ApJ*, 341, 808

Maxfield L. et al., in preparation, (Mprep)

McCarthy P. J., Spinrad H., van Breugel W., Liebert J., Dickinson M., Djorgovski S., Eisenhardt P., 1990, *ApJ*, 365, 487, (MS90)

McCarthy P. J., Spinrad H., van Breugel W., 1995, *ApJS*, 99, 27, (MSvB95)

McCarthy P. J., Miley G. K., de Koff S., Baum S. A., Sparks W. B., Golombek D., Biretta J., Macchetto F., 1997, *ApJS*, 112, 415, (McC97)

McLure R. J., Dunlop J. S., 2000, *MNRAS*, submitted, astro-ph/9908214

McLure R. J., Kukula M. J., Dunlop J. S., Baum S. A., O'Dea C. P., Hughes D. H., 1999, *MNRAS*, 308, 377

Meisenheimer K., Heavens A. F., 1986, *Nature*, 323, 419

Miley G. K., Chambers K. C., van Breugel W. J. M., Macchetto F., 1992, *ApJ*, 401, L69

Murgia M., Fanti C., Fanti R., Gregorini L., Klein U., Mack K.-H., Vigotti M., 1999, *A&A*, 345, 769

Muxlow T. W. B., Pelletier G., Roland J., 1988, *A&A*, 206, 237

Naundorf C. E., Alexander P., Riley J. M., Eales S. A., 1992, *MNRAS*, 258, 647, (NAR92)

Nolan L. A., Dunlop J. S., Kukula M. J., Hughes D. H., Boroson T., Jimenez R., 2000, *MNRAS*, to be published, astro-ph/0002020

Omont A., McMahon R. G., Cox P., Kreysa E., Bergeron J., Pajot F., Storrie-Lombardi L. J., 1996, *A&A*, 315, 1

Oort M. J. A., van Langevelde H. J., 1987, *A&AS*, 71, 25, (OvL87)

Oort M. J. A., Katgert P., Steeman F. W. M., Windhorst R. A., 1987, *A&A*, 179, 41, (OKS87)

Perlmutter S. et al., 1999, *ApJ*, 517, 565

Pilkington J. D. H., Scott P. F., 1965, *MmRAS*, 69, 183, (PS65)

Rawlings S., Eales S., Warren S., 1990, *MNRAS*, 243, L14, (REW90)

Rawlings S., Lacy M., Blundell K. M., Eales S. A., Bunker A. J., Garrington S. T., 1996a, *Nature*, 383, 502, (RLB96)

Rawlings S., Lacy M., Leahy J. P., Dunlop J. S., Garrington S. T., Lüdke E., 1996b, *MNRAS*, 279, L13, (RLL96)

Rawlings S., Eales S., Lacy M., 2000, *MNRAS*, submitted, (REL00)

Rengelink R. B., Tang Y., de Bruyn A. G., Miley G. K., Bremer M. N., Röttgering H. J. A., Bremer M. A. R., 1997, *A&AS*, 124, 259, (WENSS)

Ridgway S. E., Stockton A., 1997, *AJ*, 114, 511, (RS97)

Robson E. I., Leeuw L. L., Stevens J. A., Holland W. S., 1998, *MNRAS*, 301, 935

Röttgering H. J. A., Miley G. K., Chambers K. C., Macchetto F., 1995, *A&AS*, 114, 51, (RMC95)

Röttgering H. J. A., van Ojik R., Miley G. K., Chambers K. C., van Breugel W. J. M., de Koff S., 1997, *A&A*, 326, 505, (RvO97)

Rudnick L., Jones T. W., Fiedler R., 1986, *AJ*, 91, 1011

Smail I., Ivison R., Blain A., Kneib J.-P., Owen F., 2000a, in van Breugel W., Bland-Hawthorn J., eds, *ASP Conf. Ser.* 195: *Imaging the Universe in Three Dimensions*. p. 248

Smail I., Ivison R. J., Owen F. N., Blain A. W., Kneib J. ., 2000b, *ApJ*, 528, 612

Smith H. E., Junkkarinen V. T., Spinrad H., Grueff G., Vigotti M., 1979, *ApJ*, 231, 307, (SJ79)

Spencer R. E. et al., 1991, *MNRAS*, 250, 225

Spinrad H., private communication, (Spriv)

Spinrad H., unpublished, (S-unpub)

Spinrad H., 1982, *PASP*, 94, 397, (S82)

Spinrad H., Djorgovski S., 1984a, *ApJ*, 280, L9, (SD84a)

Spinrad H., Djorgovski S., 1984b, *ApJ*, 285, L49, (SD84b)

Spinrad H., Djorgovski S., Marr J., Aguilar L., 1985, *PASP*, 97, 932, (SDM85)

Spinrad H., Dey A., Graham J. R., 1995, *ApJ*, 438, L51, (SDG95)

Steidel C. C., Adelberger K. L., Giavalisco M., Dickinson M., Pettini M., 1999, *ApJ*, 519, 1

Stern D., Dey A., Spinrad H., Maxfield L., Dickinson M., Schlegel D., González R. A., 1999, *AJ*, 117, 1122, (SDS99)

Strom R. G., Riley J. M., Spinrad H., van Breugel W. J. M., Djorgovski S., Liebert J., McCarthy P. J., 1990, *A&A*, 227, 19, (SRS90)

Tielens A. G. G. M., Miley G. K., Willis A. G., 1979, *A&AS*, 35, 153, (TMW79)

van Breugel W. J. M., Fanti C., Fanti R., Stanghellini C., Schilizzi R. T., Spencer R. E., 1992, *A&A*, 256, 56, (vBF92)

van Breugel W. J. M., Stanford S. A., Spinrad H., Stern D., Graham J. R., 1998, *ApJ*, 502, 614, (vBS98)

van Ojik R., Röttgering H. J. A., Carilli C. L., Miley G. K., Bremer M. N., Macchetto F., 1996, *A&A*, 313, 25, (vOR96)

Veron M. P., Veron P., Witzel A., 1972, *A&A*, 18, 82

Waddington I., 1999, *The cosmological evolution of galaxies*, Ph.D. thesis, University of Edinburgh, (Wthesis)

Waddington I., Windhorst R. A., Dunlop J. S., Koo D. C., Peacock J. A., 2000, *MNRAS*, accepted, astro-ph/0006169

Waldrum E. M., Yates J. A., Riley J. M., Warner P. J., 1996, *MNRAS*, 282, 779, (WYR96)

White R. L., Becker R. H., 1992, *ApJS*, 79, 331, (WB92)

Willott C. J., Rawlings S., Blundell K. M., Lacy M., 1999, *MNRAS*, 309, 1017

Willott C. J., et al. 2000, *MNRAS*, to be submitted, (W7CRS)

Windhorst R. A., van Heerde G. M., Katgert P., 1984, *A&AS*, 58, 1, (WvHK84)

Windhorst R. A. et al., 1991, *ApJ*, 380, 362, (WBM91)

Wright A., Otrupcek R., 1990, *Parkes Catalog. Australia Telescope National Facility*, (P90)

APPENDIX A: RADIO-SUBMILLIMETRE SPECTRAL ENERGY DISTRIBUTIONS

We applied two fits to the radio spectra of our sample:

1) Linear Fit - In log-space, a straight line is fitted to radio data with $\nu > 1$ GHz. For all galaxies in the sample, at least two data points satisfy this condition. Except for the noticeably curved spectra of 3C324, MG1744+18, 4C23.56, and MG1016+058, the straight-line fit seems to mimic the existing high-frequency data very well.

2) Parabolic Fit - A physical model of synchrotron ageing could be applied to the spectra in order to determine how they might steepen. However, the fit is only required to accurately predict the shape of the expected steepening; the physics of the ageing synchrotron population does not need to be extracted from the fit. Blundell et al. (1999) have studied the properties and evolution of over 300 FRII radio sources selected from the 3C, 6C, and 7C surveys. They applied a Bayesian polynomial regression analysis to the fitting the flux densities. The process involved fitting polynomials of different degrees and associating a likelihood or probability to each. In some cases a first-order polynomial, or straight-line was the preferred choice. However, in most cases a second-order polynomial, or parabola, accurately modelled the curvature of the spectrum. A parabolic fit seems to be the best way of parameterising the curvature, as higher-order polynomials were never chosen by the regression analysis. Thus a polynomial of degree $m = 2$ was fitted, in log space, to the entire radio spectrum.

The best-fit parameters of the two models are shown in Table A1.

For each galaxy in the sample, the radio-submillimetre spectral energy distribution (SED) is presented in Figure A. The SEDs are arranged in redshift order. The solid circles denote integrated continuum flux densities. The open circles indicate radio core flux densities. For 3C356, two ra-

Table A1. Best-fit parameters (including the reduced χ^2 of the fit) of both straight-line and parabolic fits to the radio spectra (the fits were made in log-space). Note, the linear fits were applied to $\nu > 1$ GHz observations only. In addition, if only two data points were available (i.e. zero degrees of freedom), the slope and y-intercept of the line joining the two data points were calculated instead of using a fitting algorithm. No value of χ^2_{red} is given in this case. Finally, all best-fit parameters are quoted to two decimal places; therefore errors less than 0.005 are quoted as being 0.00.

Source	Linear Fit: $y = mx + k$			Parabolic Fit: $y = ax^2 + bx + c$			
	m	k	χ^2_{red}	a	b	c	χ^2_{red}
3C277.2	-1.00 ± 0.03	0.41 ± 0.02	2.8	-0.03 ± 0.02	-0.96 ± 0.01	0.40 ± 0.01	1.7
3C340	-1.03 ± 0.02	0.56 ± 0.01	2.9	-0.12 ± 0.01	-0.86 ± 0.01	0.51 ± 0.01	2.8
3C265	-1.14 ± 0.03	0.63 ± 0.01	1.3	-0.07 ± 0.01	-1.05 ± 0.01	0.60 ± 0.01	0.9
3C217	-1.24 ± 0.03	0.52 ± 0.01	2.3	-0.16 ± 0.02	-1.02 ± 0.01	0.48 ± 0.01	2.5
3C356	-1.17 ± 0.06	0.33 ± 0.04	1.3	-0.09 ± 0.02	-1.10 ± 0.02	0.32 ± 0.01	1.1
3C368	-1.34 ± 0.10	0.23 ± 0.05	0.2	-0.13 ± 0.03	-1.34 ± 0.03	0.26 ± 0.02	1.8
3C267	-0.94 ± 0.03	0.49 ± 0.02	2.9	-0.04 ± 0.01	-0.92 ± 0.01	0.50 ± 0.01	1.3
3C324	-1.20 ± 0.02	0.59 ± 0.01	5.6	-0.15 ± 0.01	-1.01 ± 0.01	0.55 ± 0.01	1.8
3C266	-1.09 ± 0.04	0.30 ± 0.03	4.0	-0.06 ± 0.02	-1.04 ± 0.01	0.31 ± 0.01	3.9
4C13.66	-1.25 ± 0.08	0.42 ± 0.04	1.2	-0.25 ± 0.04	-1.04 ± 0.03	0.39 ± 0.02	1.4
3C437	-0.95 ± 0.02	0.58 ± 0.01	0.5	-0.11 ± 0.01	-0.83 ± 0.01	0.57 ± 0.01	6.2
3C241	-1.32 ± 0.05	0.43 ± 0.02	0.2	-0.20 ± 0.03	-1.09 ± 0.02	0.38 ± 0.01	0.5
6C0919+38	-1.16	-0.36	-	-0.09 ± 0.04	-1.06 ± 0.03	-0.37 ± 0.00	0.1
3C470	-1.15 ± 0.03	0.50 ± 0.01	2.9	-0.14 ± 0.01	-0.94 ± 0.01	0.45 ± 0.01	6.0
3C322	-1.18 ± 0.05	0.46 ± 0.03	0.8	-0.10 ± 0.02	-0.99 ± 0.02	0.39 ± 0.01	2.3
6C1204+37	-1.17	-0.04	-	-0.40 ± 0.03	-1.10 ± 0.02	-0.04 ± 0.00	22
3C239	-1.22 ± 0.05	0.34 ± 0.02	0.1	-0.09 ± 0.02	-1.13 ± 0.02	0.34 ± 0.01	0.5
3C294	-1.32 ± 0.05	0.32 ± 0.03	0.3	-0.07 ± 0.02	-1.16 ± 0.02	0.26 ± 0.01	2.7
6C0820+36	-1.14	-0.40	-	-0.17 ± 0.05	-1.09 ± 0.03	-0.40 ± 0.01	2.2
6C0905+39	-1.50	-0.37	-	-0.09 ± 0.04	-1.13 ± 0.03	-0.42 ± 0.01	7.4
6C0901+35	-1.17	-0.44	-	-0.23 ± 0.04	-1.12 ± 0.03	-0.44 ± 0.01	7.7
5C7.269	-0.98	-1.03	-	-0.01 ± 0.10	-0.98 ± 0.06	-1.03 ± 0.01	0.1
4C40.36	-1.62 ± 0.03	-0.06 ± 0.02	0.7	-0.23 ± 0.03	-1.38 ± 0.02	-0.10 ± 0.01	0.2
MG1744+18	-1.16 ± 0.00	0.30 ± 0.00	335	-0.14 ± 0.00	-0.94 ± 0.00	0.22 ± 0.00	62
MG1248+11	-1.27	-0.34	-	-0.41 ± 0.15	-0.96 ± 0.04	-0.36 ± 0.04	0.9
4C48.48	-1.19 ± 0.04	-0.28 ± 0.02	0.8	-0.10 ± 0.03	-1.10 ± 0.01	-0.29 ± 0.01	0.8
53W002	-1.26 ± 0.05	-1.11 ± 0.02	0.5	-0.09 ± 0.04	-1.15 ± 0.03	-1.13 ± 0.01	0.5
6C0930+38	-1.00	-0.40	-	-0.10 ± 0.04	-0.99 ± 0.02	-0.39 ± 0.01	3.5
6C1113+34	-1.14	-0.23	-	-0.29 ± 0.04	-0.98 ± 0.03	-0.24 ± 0.00	3.9
MG2305+03	-0.97 ± 0.09	-0.15 ± 0.05	0.2	-0.02 ± 0.14	-0.95 ± 0.05	-0.15 ± 0.03	0.2
3C257	-1.03 ± 0.06	0.39 ± 0.03	0.4	-0.12 ± 0.04	-0.92 ± 0.02	0.37 ± 0.02	0.3
4C23.56	-1.40 ± 0.03	-0.19 ± 0.02	18	-0.16 ± 0.02	-1.27 ± 0.02	-0.20 ± 0.01	11
8C1039+68	-1.12	-0.44	-	-0.08 ± 0.05	-1.09 ± 0.05	-0.43 ± 0.04	0.2
MG1016+058	-1.10 ± 0.02	-0.25 ± 0.01	7.9	-0.27 ± 0.02	-0.79 ± 0.02	-0.30 ± 0.01	5.4
4C24.28	-1.31 ± 0.02	-0.08 ± 0.01	0.8	-0.15 ± 0.02	-1.18 ± 0.01	-0.09 ± 0.00	7.9
4C28.58	-1.50 ± 0.04	-0.40 ± 0.02	2.0	-0.16 ± 0.05	-1.37 ± 0.03	-0.41 ± 0.02	2.3
6C1232+39	-1.70 ± 0.00	-0.23 ± 0.00	659	-0.30 ± 0.00	-1.29 ± 0.00	-0.37 ± 0.00	25
6C1159+36	-1.11	-0.27	-	-0.34 ± 0.04	-1.03 ± 0.03	-0.27 ± 0.01	19
6C0902+34	-0.96	-0.33	-	-0.14 ± 0.03	-0.93 ± 0.02	-0.34 ± 0.00	2.5
TX1243+036	-1.31 ± 0.06	-0.32 ± 0.04	2.9	-0.08 ± 0.06	-1.33 ± 0.03	-0.27 ± 0.02	3.4
MG2141+192	-1.57 ± 0.00	-0.12 ± 0.00	25	-0.27 ± 0.02	-1.14 ± 0.02	-0.29 ± 0.01	11
6C0032+412	-1.12 ± 0.03	-0.85 ± 0.02	0.3	0.03 ± 0.02	-1.14 ± 0.01	-0.85 ± 0.01	0.7
4C60.07	-1.48 ± 0.03	-0.60 ± 0.02	0.4	-0.05 ± 0.02	-1.44 ± 0.01	-0.60 ± 0.01	0.7
4C41.17	-1.49 ± 0.03	-0.41 ± 0.02	1.6	-0.15 ± 0.02	-1.33 ± 0.01	-0.44 ± 0.01	1.1
8C1435+635	-1.85 ± 0.00	0.09 ± 0.00	4.3	-0.35 ± 0.01	-1.30 ± 0.01	-0.12 ± 0.00	3.3
6C0140+326	-1.39 ± 0.02	-0.83 ± 0.01	4.4	-0.19 ± 0.02	-1.21 ± 0.01	-0.86 ± 0.01	1.1

dio core identifications exist. The fainter core is denoted by open stars. If errors were unavailable, the error was taken to be 10 per cent of the flux density. Upper limits have been taken at the 3- σ level if $S/N < 3$. The two models fit to the data are also displayed in Figure A. The solid line is the parabolic fit to the spectrum, and the dash-dot line is the linear fit. The references for the data are: **3C277.2** - BRR00, LP; **3C340** - BRR00, LP; **3C265** - BRR00, LP; **3C217** - BRR00, LP; **3C356** -

BLR97, F93, LP; **3C368** - BLR97, BRR00, LP; **3C267** - BLR97, BRR00, LP; **3C324** - BCG98, BRB98, LP; **3C266** - BLR97, BRR00, LP, LPR92; **4C13.66** - BWE91, GC91, BRR00, LML81, LRL, P90, WB92; **3C437** - BRR00, LP; **3C241** - ASZ91, LP, vBF92; **6C0919+38** - 6C-II, CC98, FGT85, GC91, GSDC96; **3C470** - BLR97, LP; **3C322** - BRR00, LP; **6C1204+37** - 6C-II, CC98, DBB96, GC91, GSDC96, LLA95; **3C239** - BRR00, LP; **3C294** - BRR00, LP; **6C0820+36** - 6C-VI, CC98, DBB96, GC91, GSDC96,

LLA95; **6C0905+39** - 6C-II, CC98, DBB96, FGT85, GC91, GSDC96, LGE95; **6C0901+35** - 6C-II, CC98, DBB96, GC91, GSDC96, NAR92(1992); **5C7.269** - BRR00, CC98, DBB96, GSDC96; **4C40.36** - C&C69, CMvB96, CRvO97, FGT85, TMW79, WENSS; **MG1744+18** - BWE91, CRvO97, GC91, GSW67, KB17, LML81, P90, WB92; **MG1248+11** - DBB96, LML81, LBH86, WB92; **4C48.48** - 6C-V, CMvB96, CRvO97, GSW67, TMW79, WENSS; **53W002** - 6C-II, HDR97, WBM91, WvHK84, OKS87, OvL87; **6C0930+38** - 6C-II, CC98, DBB96, FGT85, GC91, GSDC96, NAR92(1992); **6C1113+34** - 6C-II, CC98, DBB96, GC91, GSDC96, LLA95A; **MG2305+03** - BWE91, GC91, GWBE95, LML81, P90, WB92; **3C257** - BWE91, CC98, DBB96, GC91, GSW67, GWBE95, HDR97, LML81, P90, vBS98, WB92; **4C23.56** - CMvB96, CRvO97, P90, PS65, TMW79; **8C1039+68** - HWR95, Lthesis; **MG1016+058** - BWE91, CC98, CFR98, DBB96, DSD95, GC91, GSW67, GWBE95, LML81, P90, WB92; **4C24.28** - CMvB96, CRvO97, P90, PS65, TMW79, WYR96; **4C28.58** - CC98, CMvB96, DBB96, PS65, TMW79; **6C1232+39** - 6C-II, CC98, C&K94, CRvO97, DBB96, FGT85, GC91, GSDC96, NAR92(1992); **6C1159+36** - 6C-II, CC98, DBB96, GC91, GSDC96, LLA95; **6C0902+34** - 6C-II, C95, CC98, C&K94, COH94, DBB96, DSS96, GC91, GSDC96, HDR97, LLA95; **TX1243+036** - CC98, CFR98, DBB96, GSW67, LML81, P90, vOR96, WB92; **MG2141+192** - BWE91, CC98, CRvO97, DBB96, GC91, GSW67, HDR97, WB92; **6C0032+412** - 6C-VI, BRE98, DBB96, FGT85, GC91, GSDC96, HDR97; **4C60.07** - 6C-V, CC98, CMvB96, CRvO97, DBB96, TMW79, WENSS; **4C41.17** - 6C-VI, BCO99, CC98, C&K94, CMvB90, COH94, DBB96, DHR94, FGT85, GSW67, TMW79, WENSS; **8C1435+635** - 6C-III, CC98, CRvO97, DBB96, HDR97, HWR95, I95, IDHA98, LMR94; **6C0140+326** - 6C-VI, BRE98, CC98, DBB96, FGT85, RLB96.

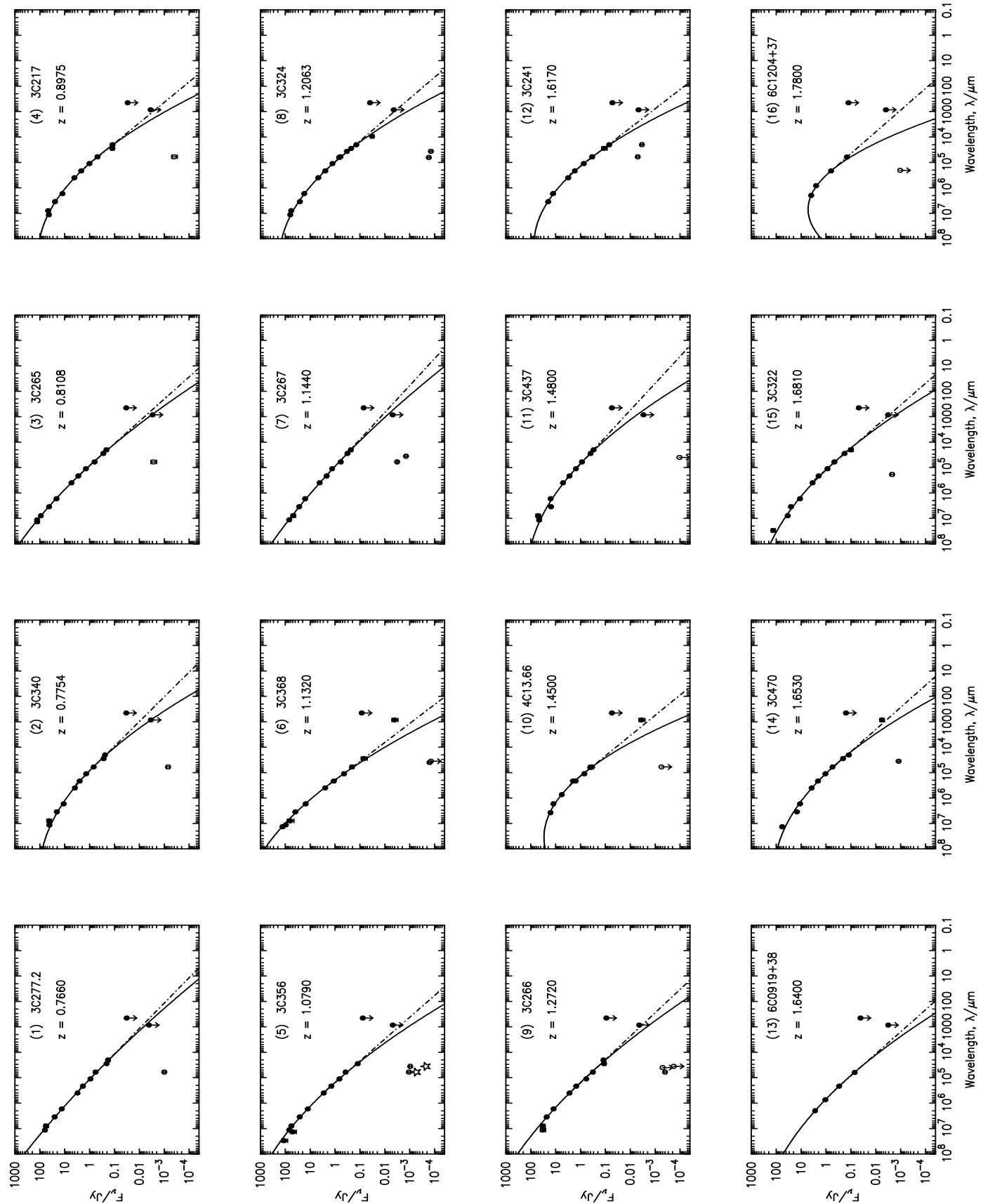
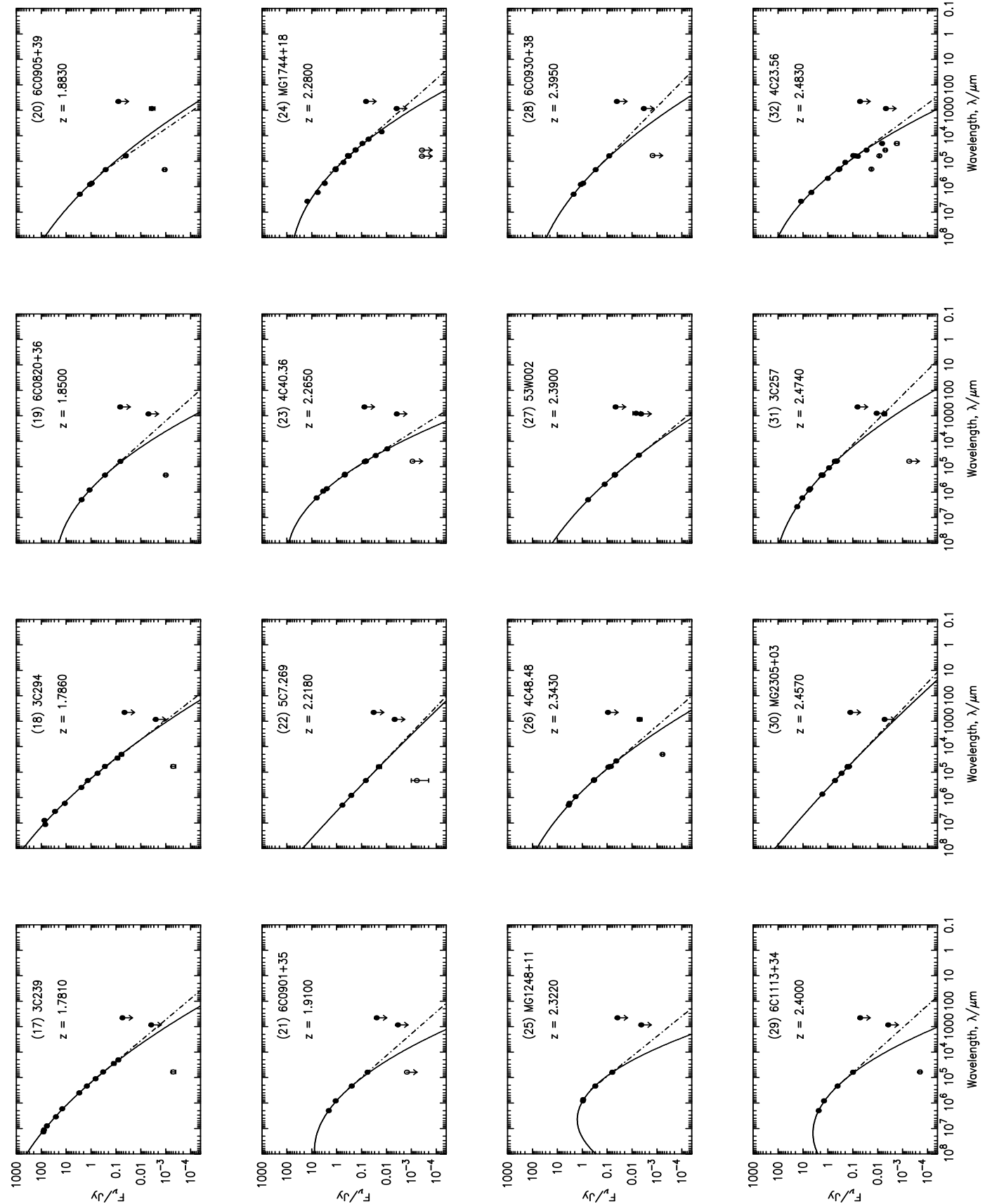


Figure A1. Spectral Energy Distributions



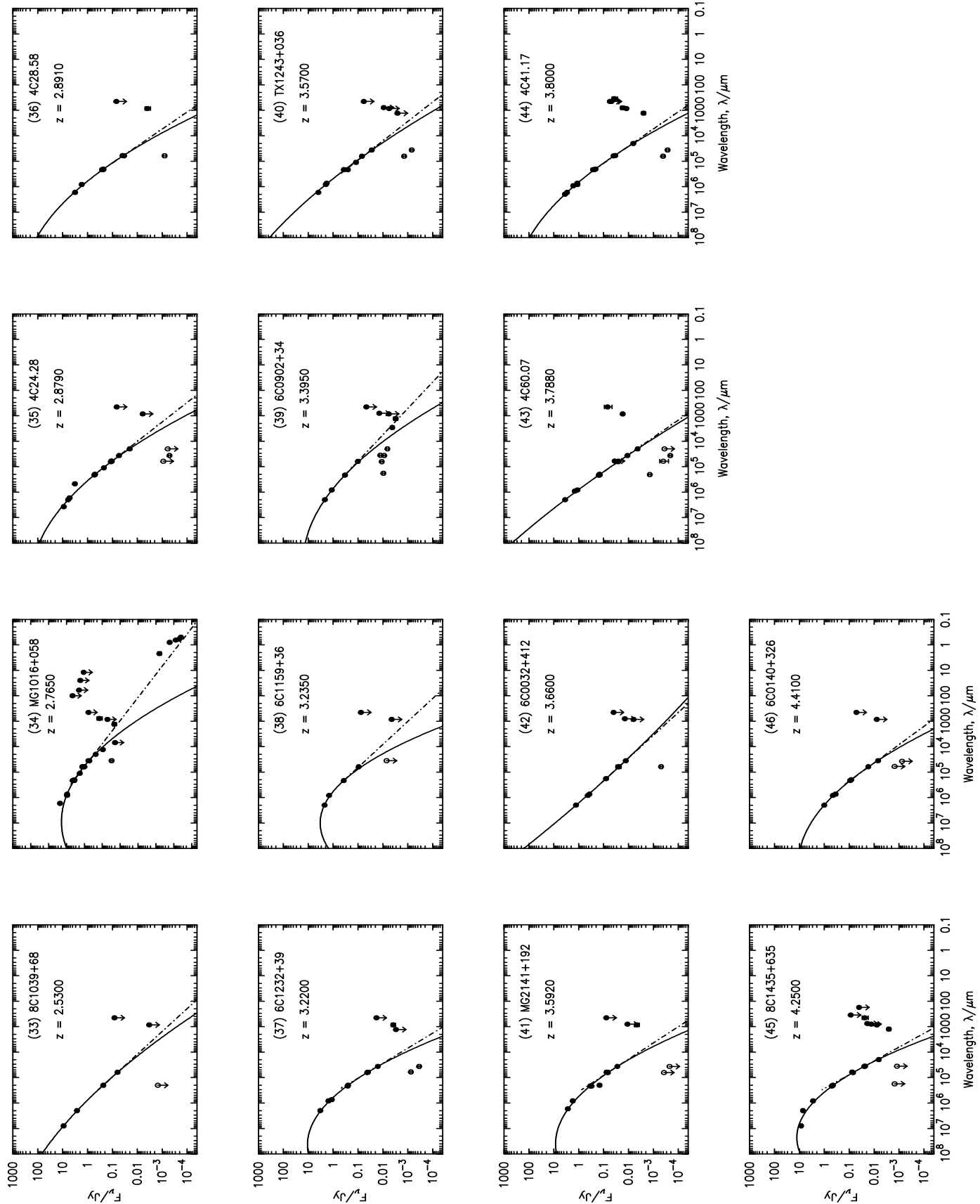


Figure A1 – *continued*